Journal of Volcanology and Geothermal Research 295 (2015) 26–42

Contents lists available at ScienceDirect

Journal of Volcanology and Geothermal Research

journal homepage: www.elsevier.com/locate/jvolgeores

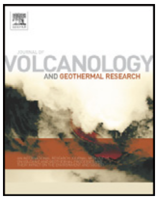

Mechanical behaviour and failure modes in the Whakaari (White Island volcano) hydrothermal system, New Zealand

Michael J. Heap [a,*], Ben M. Kennedy [b], Noémie Pernin [a], Laura Jacquemard [a], Patrick Baud [a], Jamie I. Farquharson [a], Bettina Scheu [c], Yan Lavallée [d], H. Albert Gilg [e], Mark Letham-Brake [b,f], Klaus Mayer [c], Arthur D. Jolly [g], Thierry Reuschlé [a], Donald B. Dingwell [c]

[a] Géophysique Expérimentale, Institut de Physique de Globe de Strasbourg (UMR 7516 CNRS, Université de Strasbourg/EOST), 5 rue René Descartes, 67084 Strasbourg Cedex, France
[b] Geological Sciences, University of Canterbury, Private Bag 4800, 8140 Christchurch, New Zealand
[c] Department for Earth and Environmental Sciences, Ludwig-Maximilians-Universität, Munich, Theresienstr.41/III, 80333 Munich, Germany
[d] Earth, Ocean and Ecological Sciences, University of Liverpool, Liverpool L69 3GP, United Kingdom
[e] Lehrstuhl für Ingenieurgeologie, Technische Universität München, Arcisstr. 21, 80333 Munich, Germany
[f] Kakapo Disaster Resilience Trust, 7/63 Brockworth Place, Riccarton, Christchurch 8011, New Zealand
[g] GNS Science, Whakaari Research Centre, Private Bag 2000, Taupo 3330, New Zealand

ARTICLE INFO

Article history:
Received 23 October 2014
Accepted 27 February 2015
Available online 10 March 2015

Keywords:
Dilatant
Compaction
Structural stability
Seismicity
Shear fracture
Pore collapse

ABSTRACT

Volcanic hydrothermal systems host a prodigious variety of physico-chemical conditions. The physico-chemical state and mechanical behaviour of rocks within is correspondingly complex and often characterised by vast heterogeneity. Here, we present uniaxial and triaxial compression experiments designed to investigate the breadth of mechanical behaviour and failure modes (dilatant or compactant) for hydrothermally-altered lava and ash tuff deposits from Whakaari (White Island volcano) in New Zealand, a volcano with a well-documented and very active hydrothermal system. Our deformation experiments show that the failure mode of low porosity lava remains dilatant over a range of depths (up to pressures corresponding to depths of about 2 km). Upon failure, shear fractures, the result of the coalescence of dilatational microcracks, are universally present. The high porosity ash tuffs switch however from a dilatant to a compactant failure mode (driven by progressive distributed pore collapse) at relatively low pressure (corresponding to a depth of about 250 m). We capture the salient features of the dynamic conditions (e.g., differential stress, effective pressure) in a schematic cross section for the Whakaari hydrothermal system and map, for the different lithologies, areas susceptible to either dilatant vs. compactive modes of failure. The failure mode will impact, for example, the evolution of rock physical properties (e.g., porosity, permeability, and elastic wave velocity) and the nature of the seismicity accompanying periods of unrest. We outline accordingly the potential implications for the interpretation of seismic signals, outgassing, ground deformation, and the volcanic structural stability for Whakaari and similar hydrothermally-active volcanoes worldwide.

1. Introduction

Volcanic hydrothermal systems typically exist where water (either meteoric or marine) mixes with hot magmatic fluids and convects within porous rock and sediments. The ingress of magmatic volatile fluids can significantly lower the pH of the discharge region near the surface; often yielding an aggressive hydrothermal system as observed, for example, at Yellowstone National Park (USA, e.g., Fournier, 1989), in the Aeolian Islands (Italy, e.g., Fulignati et al., 1999), within the Taupo Volcanic Zone (New Zealand, e.g., Christensen et al., 2002), and along the Tonga–Kermadec Arc (South Pacific Ocean, e.g., Leybourne et al., 2012).

The lithostatic and pore pressure, temperature, and fluid chemistry within a volcanic hydrothermal system can vary tremendously, both in time and space (e.g., Giggenbach and Sheppard, 1989; Bonafede, 1991; Bolognesi and D'Amore, 1993; Christensen and Wood, 1993; Day, 1996). The first-order consequences of this variability are twofold. Firstly, the rocks in volcanic hydrothermal systems are often subject to a broad array of chemical alterations that can modify rock state and thereby physical properties (e.g., Browne, 1978). Secondly, the mechanical response of a rock to a differential stress is a function of both the conditions under which it deforms (i.e., variations between lithostatic and pore pressure; see Paterson and Wong, 2005) and the petrophysical properties of the system (e.g., porosity, mineralogical composition, grain size, pore size; see Wong and Baud, 2012) Thus, varying degrees of hydrothermal alteration may be expected to have a first-order impact

---

* Corresponding author.
E-mail address: heap@unistra.fr (M.J. Heap).

http://dx.doi.org/10.1016/j.jvolgeores.2015.02.012

on the strength and failure mode of rock, and initially homogeneous rocks may exhibit different failure modes depending on their location within the volcanic hydrothermal system.

The processes leading to the hydrothermal alteration of rock include dissolution, mineral precipitation, and secondary mineralisation (e.g., Browne, 1978). For volcanic rocks, hydrothermal alteration typically results in the formation of clay minerals (e.g., kaolinite, illite, smectite), sulphates (e.g., alunite, jarosite), and silica polymorphs (e.g., opal, cristobalite; Kyriakopoulos et al., 1990; Çelik et al., 1999). Experimental studies have already underscored the general weakening effect of hydrothermal alteration on rock (e.g., Watters et al., 2000; del Portro and Hürlimann, 2008, 2009; Pola et al., 2012, 2014; Siratovich et al., 2014; Wyering et al., 2014), although hydrothermal alteration at high temperatures (>200 °C), characterised by pore- and crack-filling precipitation, may increase rock strength (Wyering et al., 2014). On a larger scale, pervasive hydrothermal alteration has been blamed for structurally destabilising a volcanic system, making it more susceptible to catastrophic collapse (e.g., Lopez and Williams, 1993; Watters et al., 2000; Reid et al., 2001; Finn et al., 2007; John et al., 2008; Procter et al., 2014).

As noted above, the mechanical response and failure mode of rock depends on its physical characteristics (e.g., porosity, pore size, etc.) and the conditions under which it deforms (lithostatic and pore pressure, temperature) (Paterson and Wong, 2005; Wong and Baud, 2012). The effective pressure (the confining pressure minus the pore pressure) is a dominating influence governing the mechanical behaviour of the rock. The failure mode of low porosity rocks is typically dilatant, even at considerable effective pressures/depths (e.g., Brace, 1964). Porous rocks however can switch from a dilatant to a compactive response at relatively low effective pressures or shallow depths (Wong and Baud, 2012). A switch from a dilatant to a compactant mode of failure has been previously observed in porous volcanic rock: dacite from Augustine volcano (USA) (Kennedy et al., 2009), tuff from the Alban Hills (Italy) (Zhu et al., 2011), trachyandesite (Loaiza et al., 2012), basalt (Adelinet et al., 2013), and andesites from Volcán de Colima (Mexico) (Heap et al., submitted for publication). The interest here is that the accumulation of inelastic deformation (damage) and the failure mode (dilatant vs. compactant) can in turn influence the evolution of rock physical properties. Compactive deformation leads to a porosity decrease (e.g., Wong and Baud, 2012), an increase in elastic wave velocities (e.g., Fortin et al., 2005), and a decrease in permeability (e.g., David et al., 1994; Fortin et al., 2005; Baud et al., 2012; Heap et al., submitted for publication). In contrast, dilatant behaviour is accompanied by an increase in porosity (e.g., Read et al., 1995), a decrease in elastic wave velocities (e.g., Ayling et al., 1995), and, for low porosity rock, an increase in permeability (e.g., Nara et al., 2011), although we note that high porosity rocks may suffer a reduction in permeability in the dilatant regime (e.g., Zhu and Wong, 1997). The different failure modes also have different acoustic emission (AE) signatures: dilatant failure, shear fracture formation, is characterised by the acceleration of predominately shear events as failure is approached, while compactive failure, cataclastic flow and compaction localisation, is accompanied by a more continuous accumulation of predominately compaction events (Wong et al., 1997; Fortin et al., 2009).

And so it is that, especially for the case of hydrothermally-altered rock, an understanding of the breadth of deformation and failure modes, and their potential impact on rock physical properties, is of prime interest in volcano stability assessment (e.g., Reid et al., 2001) as well as the interpretation of volcano-seismic signals (e.g., Sherburn et al., 1998; Bean et al., 2014). A natural consequence is that rock physical properties are a crucial input for mechanistic models of the geophysical signals of volcano unrest (e.g., Manconi et al., 2010; Todesco et al., 2010; Fournier and Chardot, 2012; Heap et al., 2014a) and they may govern the efficacy of magmatic conduit outgassing, with its consequences for the explosivity and magnitude of volcanic eruptions (e.g., Eichelberger et al., 1986; Woods and Koyaguchi, 1994; Jaupart, 1998; Mueller et al., 2008; Heap et al., 2014b, submitted for publication). Here therefore we explore the mechanical behaviour of a suite of hydrothermally-altered volcanic rocks from Whakaari (White Island volcano) in New Zealand, a well-investigated natural laboratory of a volcanic hydrothermal system. The micromechanical mechanisms responsible for dilatant and compactive behaviour are examined and the potential implications for Whakaari, and other volcanic hydrothermal volcanoes worldwide, are discussed.

2. Case study: Whakaari (White Island volcano)

Whakaari is an active andesite–dacite stratovolcano situated within the Taupo Volcanic Zone (TVZ), approximately 50 km north from the coast of New Zealand's North Island (Fig. 1). Although the subaerial expression of Whakaari is relatively modest (summiting at 321 m above sea level and measuring 2.4 km west–east by 2 km north–south) it nonetheless represents merely the tip of a much larger submarine structure (Clark and Cole, 1986; Houghton and Nairn, 1991 and references therein). The island comprises two overlapping, predominantly andesitic cones (the Ngatoro Cone and Central Cone) composed of historic lava flows, agglomerates, tuffs, tephras, and breccias (Cole et al., 2000 and references therein). Whakaari hosts an open, highly reactive hydrothermal system (Giggenbach et al., 2003 and references therein), with a surface expression of hot springs and mud pools, fumaroles, and acid streams and lakes. A large lake of boiling acidic waters in the western subcrater—crater lake—marks the present day centre for volcanic activity and outgassing (e.g., Werner et al., 2008; Bloomberg et al., 2014).

The eruptive behaviour of Whakaari is typically characterised by frequent, small phreatic and phreatomagmatic eruptions (e.g., Houghton and Nairn, 1989, 1991 and references therein). Most recently, a period of unrest, beginning in 2012 and ceasing around October 2013, was characterised by intermittent phreatic, phreatomagmatic, and effusive magmatic eruptions, interspersed with mud eruptions and seismic activity (Miller and Jolly, 2014). Activity at the volcano is accompanied by a broad range of seismic activity, including volcano-tectonic earthquakes, volcanic tremors, and low frequency events (e.g., Nishi et al., 1996; Sherburn et al., 1998). Further, intense swarms of low-amplitude, high-frequency events have been observed, thought to originate close to major fracture zones or areas of significantly increased permeability beneath the main crater (Nishi et al., 1996). Nishi et al. (1996) suggest that the spatial distribution of seismic activity at Whakaari is controlled by intrusion-induced thermal and mechanical stresses, as well as by a reduction in rock strength associated with the circulation of reactive hydrothermal fluids.

3. Experimental materials

We selected five hydrothermally-altered rocks from Whakaari (Fig. 2). Our samples were chosen to represent the interbedded lava deposits (hereafter referred to as "lavas") and ash tuff units exposed in the cliffs of the eastern wall of the volcanic amphitheatre near Shark Bay (Fig. 1c). The five blocks (approximately 300 × 300 × 300 mm) were sampled from the accessible scree at the foot of the eastern wall (indicated in Fig. 1c) and most likely originated from approximately 50 to 70 m beneath the current cliff top, where fresh scarps of similar rock types are exposed. This sampling site was chosen due to the wide variety of available rock types and its accessibility. As it is likely that several hundred metres of overlying material (at the top of the volcano) has been removed by prehistoric debris avalanches, we infer that these lithologies were originally buried more than 100 m beneath the surface, and that similar lithologies exist at those depths beneath the central crater today. However, lava flows may have dominated the early emergent eruption phases. If so it is possible that the proportion of lava deposits may increase with depth (Cole et al., 2000).

Cylindrical samples (20 mm in diameter) were cored from each of the five blocks collected (54 cylindrical cores were prepared in total).

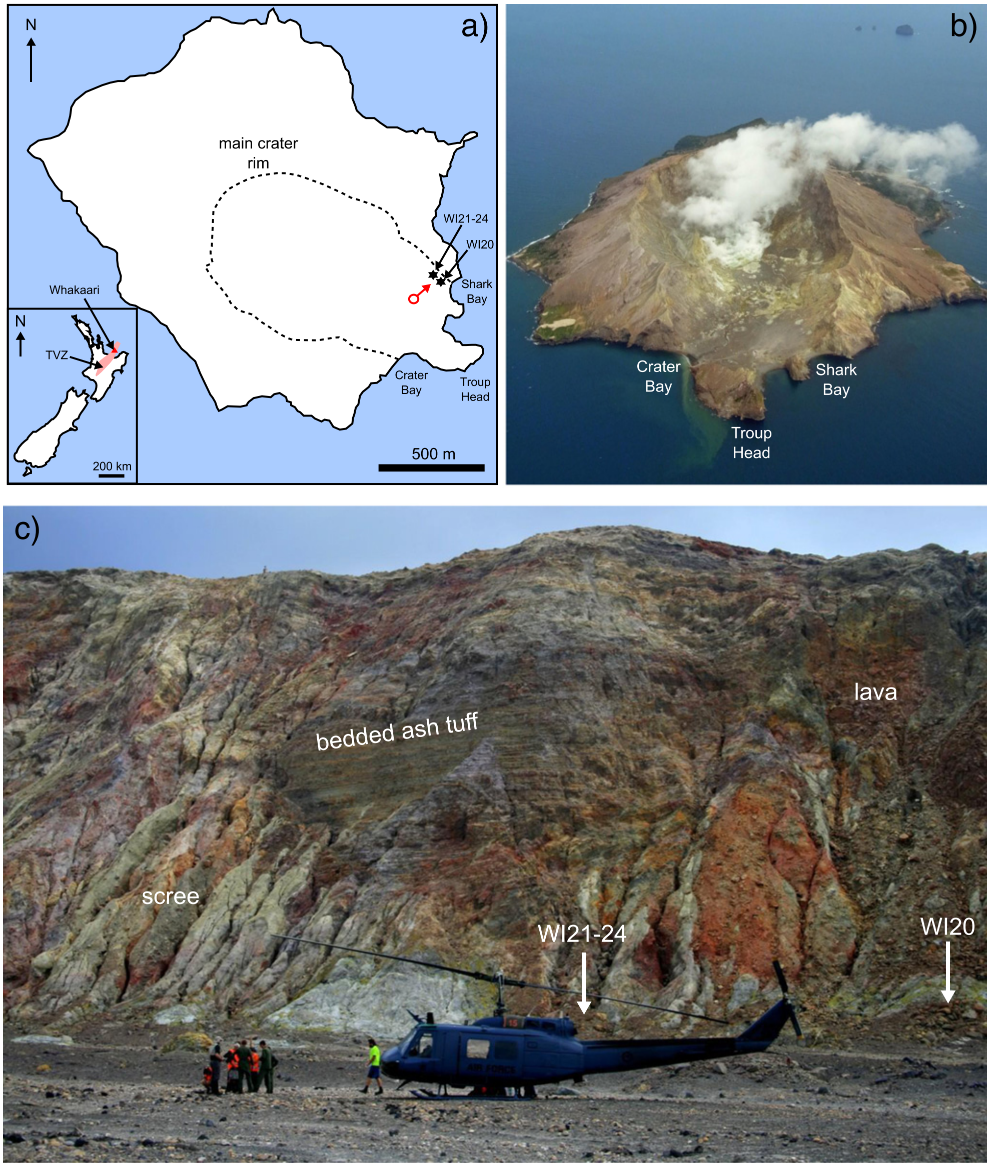

Fig. 1. Whakaari (White Island volcano). (a) Map of Whakaari showing the locations of the sample collection sites. The inset shows a map of New Zealand indicating the location of the Taupo Volcanic Zone and Whakaari. The unfilled red circle and arrow show the position and direction for the photograph shown in panel (c). (b) Aerial photograph of Whakaari (photo credit: Ben Kennedy). (c) Photograph of the crater wall showing the interbedded ash tuffs and lavas (cliff approximately 150 m high). The sample collection sites are also indicated (photo credit: Ben Kennedy).

The samples of each single block were all cored in the same orientation. The end-faces of each sample were ground flat and parallel to a nominal length of 40 mm. The connected porosity of each sample was measured using the triple-weight water saturation technique using Archimedes' principle (Guéguen and Palciauskas, 1994). Mineral composition was determined by X-ray diffraction analysis (XRD) at the Technische Universität München (Table 1). The disaggregated samples were mixed with an internal standard (10% ZnO) and ground for 8 min with 10 ml of isopropyl alcohol in a McCrone Micronising Mill using agate cylinder elements. The XRD analyses were performed on powder mounts using a PW 1800 X-ray diffractometer (CuKα, graphite monochromator, 10 mm automatic divergence slit, step-scan 0.02° 2θ increments per second, counting time 1 s per increment, 40 mA, 40 kV). The crystalline and amorphous phases in the whole rock powders were quantified using the Rietveld program BGMN (Bergmann et al., 1998). Textural analysis was performed using hand specimens as well as optical and scanning electron microscopy (SEM).

3.1. Lava deposit

The lava (WI20) collected contains an average porosity of 6.0% (porosity varies depending on the number of macroscopic cracks within the sample; Table 2). The lava is of andesitic composition ($SiO_2 = 58\%$) and likely originates from one of the competent lava units from the currently active Central Cone (see the schematic stratigraphic logs in Cole et al., 2000). Photographs and an SEM photomicrograph are shown in Fig. 2a, and reveal a porphyritic lava locally cracked and oxidised, containing phenocrysts of feldspar and pyroxene (some with altered microporous rims). The groundmass consists of hydrated amorphous glass with microlites of feldspar and pyroxene and minor iron oxides (hematite) (Fig. 2a). Pores are typically a couple of hundred microns in diameter, although smaller pores are observed along the edges of altered phenocrysts. Microcracks are abundant. Jarosite and gypsum, both alteration minerals, have precipitated into some of the pores. XRD analysis attests that WI20 is only *moderately* altered (i.e., less than half of the

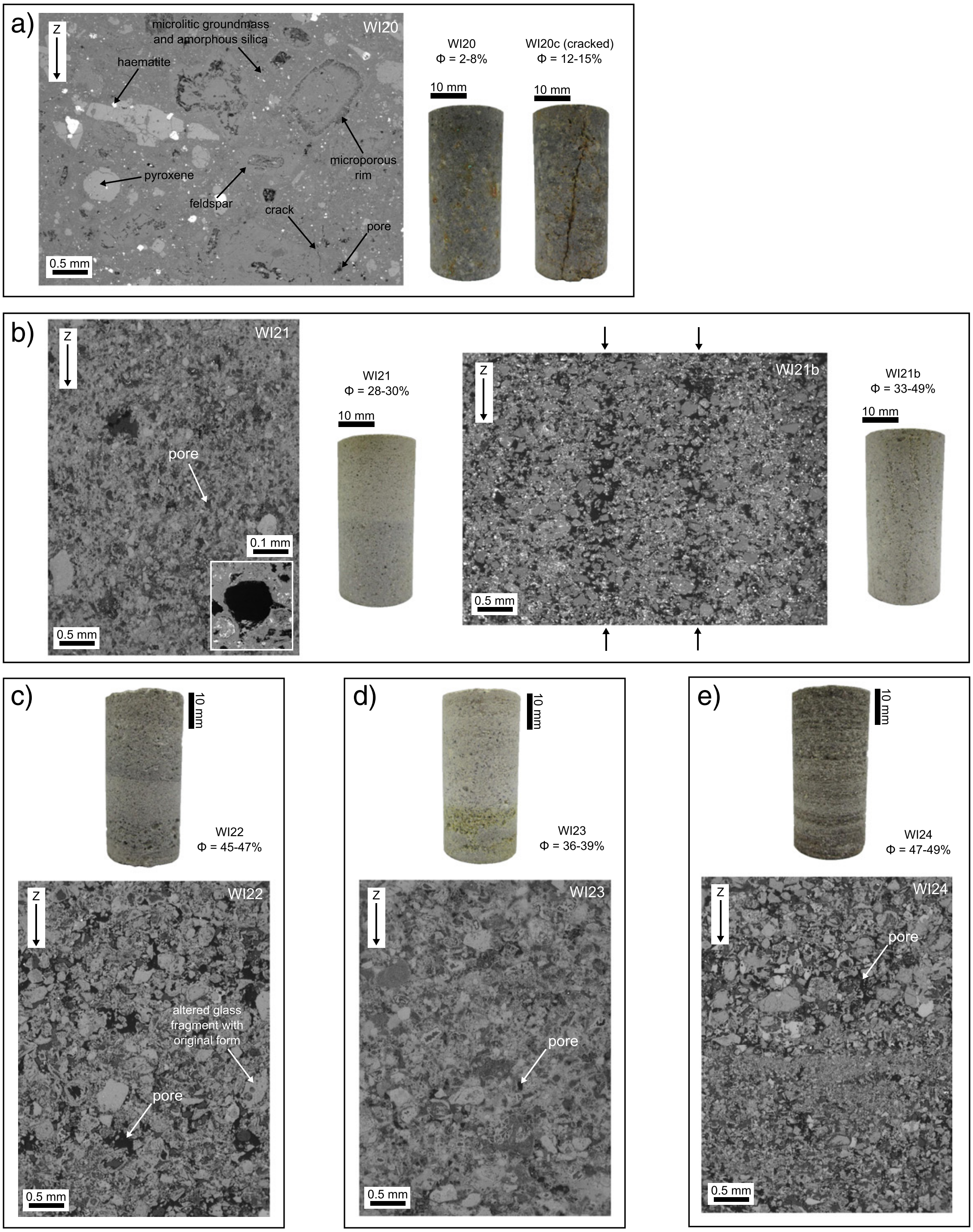

Fig. 2. Hydrothermally-altered samples. (a) SEM photomicrograph (uncracked) and sample pictures for WI20 (uncracked, WI20, and cracked, WI20c). (a) SEM photomicrograph and sample picture for WI21 (inset shows a zoomed image of a typical pore) and WI21b. The gas elutriation pipes of WI21b are indicated with arrows on the SEM image. SEM photomicrographs and sample pictures are also provided for WI22 (c), WI23 (d), and WI24 (e). Porosity ranges are given next to each sample.

mineral phases have been altered or replaced; classified following British Standard practice (BS5930, 1999); see also Pola et al., 2012) and is composed of plagioclase (37%), K-feldspar (14%), pyroxene (10%), cristobalite (17%), amorphous phases, mostly volcanic glass and possibly some opal-A (14%), gypsum (4%), jarosite (3%), and haematite (1%).

3.2. Ash tuff deposits

Four ash tuff deposits were selected based on observable differences in colour (type of alteration), macroscopic texture (presence/absence of bedding and gas elutriation pipes), particle size, and degree of cementation (Fig. 2b–e). All of the ash tuffs are composed of partially-cemented ash particles (i.e., <2 mm). The ash particles are altered crystal fragments and completely devitrified shards of glass, now composed dominantly of hydrated amorphous silica (opal-A). The deposits are therefore classified as crystal-vitric ash tuffs or, for brevity, “ash tuffs”. Although some of the altered glass (Fig. 2c) and crystal fragments (Fig. 3a) retain their original morphology, the original fragments and shards are often difficult to distinguish from the opal-A and the alunite (where present) that now bind the rock together. Pore-filling alunite,

Table 1
X-ray diffraction (XRD) analysis showing the bulk geochemical composition of each of the studied rocks.

	WI20 WI20c	WI21 WI21b	WI22	WI23	WI24
(K, Na)-alunite	–	32 ± 3	6 ± 3	25 ± 3	1 ± 1
Jarosite	3 ± 1	–	–	4 ± 1	4 ± 1
α-Sulphur	–	–	–	–	
Gypsum	4 ± 1	1 ± 1	1 ± 1	–	–
Amorphous phases (volcanic glass, opal-A)	14 ± 5	66 ± 6	90 ± 3	68 ± 4	92 ± 2
Kaolinite	–	–	–	2 ± 2	–
Cristobalite	17 ± 4	1 ± 1	3 ± 1	1 ± 1	2 ± 1
Quartz	–	<1	<1	<1	1 ± 1
Pyroxene	10 ± 2	–	–	–	–
Plagioclase	37 ± 3	–	–	–	–
Hematite	1 ± 1	–	–	–	1 ± 1
K-feldspar	14 ± 2	–	–	–	–

present in two of the ash tuffs (Table 1), likely precipitated following complete devitrification and opal replacement (Fig. 3b). All of the ash tuffs contain pores, typically a couple of hundred microns in diameter.

Samples cored from the first ash tuff block, white/grey in colour, were split into two families: those without (WI21) and with (WI21b) gas elutriation pipes (Fig. 2b). WI21 and WI21b contain an average porosity of 29.2 and 39.7% (Table 2), respectively. Both WI20 and WI21b contain an average particle size of about 0.1 mm (although particles can be as large as 0.2 or 0.3 mm). XRD analysis shows that WI21 and WI21b are composed of amorphous phases, mostly opal-A (66%), alunite (32%), and minor quantities of gypsum, cristobalite, and quartz (Table 1). WI21 and WI21b do not contain bedding. The second block, grey in colour (WI22, Fig. 2c), contains an average porosity of 46.1% (Table 2) and is composed of opal-A (90%), alunite (6%), cristobalite (3%), and minor quantities of gypsum and quartz (Table 1). The average particle size of WI22 is about 0.3 mm. WI22 contains bedding consisting of 10 mm-thick alternating bands of high and low porosity (Fig. 2c). The third block, also white in colour (WI23, Fig. 2d), contains an average porosity of 37.3% (Table 2) and is composed of opal-A (68%), alunite (25%), jarosite (4%), kaolinite (2%), and minor quantities of cristobalite and quartz (Table 1). WI23 does not contain bedding and the average particle size is about 0.2 mm. Finally, the forth block, brown-red/grey in colour (WI24, Fig. 2e), contains an average porosity of 47.1% and is composed of opal-A (92%), jarosite (3%), cristobalite (2%), and minor quantities of alunite, quartz, and haematite (Table 1). WI24 contains alternating brown-red and grey layers (3–10 mm-thick, Fig. 2e). Some layers contain an average particle size of about 0.4 mm, while others contain an average particle size of about 0.15 mm (Fig. 2e).

Since all four of the ash tuffs contain none of their original mineral phases, they can be described as *completely* altered (BS5930, 1999; see also Pola et al., 2012), although the type of alteration differs between the samples (WI21 and WI23 contain abundant pore-filling alunite (Fig. 3b), while WI22 and WI24 do not; Table 1). The presence/absence of precipitated alunite in the ash tuffs attests to the heterogeneous nature of the alteration within the hydrothermal system at Whakaari and to the mobility of aluminium. This precludes the use of chemical alteration indices that assume aluminium immobility, such as the Chemical Index of Alteration (CIA), the Chemical Index of Weathering (CIW), or the Plagioclase Index of Alteration (PIA) for example (see Pola et al., 2012 and references therein).

4. Experimental methods

All experiments were performed at the Géophysique Expérimentale laboratory at the Institut de Physique du Globe de Strasbourg on the cylindrical samples cored from the blocks collected. The measurements and experiments of this study were performed at room temperature. These data are therefore relevant for rocks that have cooled well below their corresponding glass transition temperatures, as well as those devoid of fresh glass as a result of hydrothermal alteration, as is the case for the majority of the rocks at Whakaari. We note however, that locally high temperatures may affect the stability of some of the alteration mineral phases (e.g., clays, hydrated sulphates). A future contribution will investigate the influence of temperature on the mechanical behaviour of the hydrothermally-altered rocks at Whakaari. In this study we will adopt the convention that compressive stresses and compactive strains are positive. A summary table of the experimental conditions is provided as Table 2.

4.1. Benchtop elastic wave velocities

P-wave velocity was measured along the long axis of each of the cylindrical samples under "dry" conditions, whereby samples were vacuum-dried at a temperature of 40 °C for at least 48 h. All measurements were collected under a uniaxial stress of 1.9 MPa (i.e., $\sigma_2 = \sigma_3 = 0$).

4.2. Uniaxial deformation experiments

The unconfined compressive strength (UCS) experiments (i.e., $\sigma_1 > \sigma_2 = \sigma_3$; $\sigma_2 = \sigma_3 = 0$) of this study were performed on all sample types under a constant strain rate of 10^{-5} s^{-1} until failure. Experiments were either performed dry or "wet" (i.e., samples were vacuum-saturated with distilled water), depending on how much material was available for sampling. During deformation, axial strain and stress were continuously monitored by a displacement transducer and a load cell, respectively.

4.3. Triaxial experiments

Constant strain rate (10^{-5} s^{-1}) conventional (i.e., $\sigma_1 > \sigma_2 = \sigma_3$; $\sigma_2 = \sigma_3 > 0$) triaxial experiments were performed on samples of WI20, WI21, and WI21b. Experiments were conducted at room temperature on (distilled) water-saturated samples under a constant strain rate (and in drained conditions) until failure. In this study we adopt a simple effective pressure (Peff) law where effective pressure is defined as the confining pressure (Pc) minus the pore fluid pressure (Pp) multiplied by a constant, the Biot coefficient, which we assume here to be 1 (Guéguen and Palciauskas, 1994).

Experiments on WI20 and WI21b were performed under effective pressures of 5, 10, 20, and 30 MPa (using a constant Pp of 10 MPa), and experiments on WI21 were performed at effective pressures of 5, 10, 20, 30, 50, and 70 MPa (using a constant Pp of 10 MPa). Our triaxial experiments were performed on samples containing similar porosities (Table 2) to circumvent the problems associated with sample variability. Axial stress and strain were monitored continuously using a load cell and an LVDT displacement transducer, respectively, and pore volume change (used to interpret porosity change) was monitored using a pore pressure intensifier/volumometer. The output of AEs during deformation (to be used as a proxy for the initiation and propagation of microcracks) was monitored during six of the experiments (WI20 and WI21 at Peffs of 5, 10, 20, and 30 MPa) by a piezoelectric transducer crystal (attached to the top of the piston) using a Physical Acoustics USB AE Node. During experimentation, an AE hit was recorded if a signal exceeded the set threshold of 45 dB. The "energy" (the area under the received AE waveform) of each AE signal was provided by the AEwin software. Further information on the experimental setup can be found in Heap et al. (2014a).

Hydrostatic experiments (i.e., $\sigma_1 = \sigma_2 = \sigma_3$) were also performed on samples WI21 and WI21b. The samples were first left overnight under a confining pressure of 12 MPa and a pore fluid pressure of 10 MPa. The confining pressure was then increased at a rate of 0.003 $MPa \cdot s^{-1}$. During the experiment pore volume change

Table 2
Summary of the 54 experiments presented in this study (36 uniaxial experiments and 18 triaxial experiments). All experiments were performed at the Géophysique Expérimentale laboratory at the Institut de Physique du Globe de Strasbourg. ϕ—porosity; Vp—P-wave velocity; Pc—confining pressure; Pp—pore fluid pressure; Peff—effective pressure; Q—differential stress; P—effective mean stress; C*—onset of shear enhanced compaction; P*—onset of inelastic hydrostatic pore collapse. "WI20c"–WI20 samples containing macrocracks (see Fig. 2A); "WI21b"–WI21 samples containing gas elutriation pipes (see Fig. 2B). "Pp = 0 (wet)" refers to uniaxial experiments performed on water-saturated samples. "Hydro" refers to hydrostatic experiments.

Sample	ϕ [%]	Bulk density [kg m^{-3}]	Vp [km·s^{-1}]	Pc [MPa]	Pp [MPa]	Peff [MPa]	Q at peak stress [MPa]	Q at C* [MPa]	Peff at P* [MPa]	P [MPa]
WI20	6.6	2516	4.77	0	0	0	139.9	–	–	46.6
WI20	8.0	2472	4.55	0	0	0	143.9	–	–	48.0
WI20	7.7	2461	4.61	0	0	0	113.0	–	–	37.7
WI20c	12.3	2307	1.54	0	0	0	44.3	–	–	14.8
WI20	7.7	2478	4.85	0	0	0	139.0	–	–	46.3
WI20	1.6	2484	4.67	0	0	0	153.5	–	–	51.2
WI20c	15.3	2428	4.50	0	0	0	66.9	–	–	22.3
WI20	5.3	2514	5.08	0	0 (wet)	0	94.1	–	–	31.4
WI20	5.9	2521	5.01	15	10	5	138.4	–	–	51.1
WI20	5.9	2520	4.88	20	10	10	164.4	–	–	64.8
WI20	5.9	2522	4.96	30	10	20	211.1	–	–	90.4
WI20	6.3	2522	4.79	40	10	30	253.7	–	–	114.6
WI20	5.4	2523	4.99	Hydro.	10	Hydro.	–	–	–	–
WI21	28.1	1633	3.22	0	0 (wet)	0	56.0	–	–	18.7
WI21	29.8	1595	2.85	15	10	5	55.3	–	–	23.4
WI21	29.8	1587	2.79	20	10	10	71.2	–	–	33.7
WI21	28.9	1626	3.03	30	10	20	–	71.6	–	43.9
WI21	29.9	1596	3.08	40	10	30	–	70.2	–	53.4
WI21	27.9	1642	3.29	60	10	50	–	61.9	–	70.6
WI21	28.4	1626	3.07	80	10	70	–	49.9	–	86.6
WI21	30.8	1570	2.91	Hydro.	10	Hydro.	–	–	109.5	109.5
WI21b	42.0	1285	1.98	0	0	0	10.8	–	–	3.6
WI21b	39.3	1343	1.92	0	0	0	19.9	–	–	6.6
WI21b	41.1	1307	1.85	0	0	0	8.8	–	–	2.9
WI21b	39.5	1350	1.98	0	0	0	13.4	–	–	4.5
WI21b	43.5	1227	1.51	0	0	0	13.0	–	–	4.3
WI21b	48.7	1099	1.46	0	0	0	7.8	–	–	2.6
WI21b	44.4	1229	1.31	0	0	0	4.4	–	–	1.5
WI21b	42.5	1265	1.70	0	0 (wet)	0	9.2	–	–	3.1
WI21b	44.5	1191	1.94	0	0 (wet)	0	9.8	–	–	3.3
WI21b	41.1	1307	1.85	0	0 (wet)	0	14.1	–	–	4.7
WI21b	34.6	1469	2.38	15	10	5	24.2	–	–	13.1
WI21b	36.9	1407	1.94	20	10	10	–	13.6	–	14.5
WI21b	37.0	1451	2.67	30	10	20	–	10.9	–	23.6
WI21b	32.7	1532	2.91	40	10	30	–	12.1	–	34.0
WI21b	33.9	1472	2.34	40	10	30	–	11.5	–	33.8
WI21b	32.9	1525	2.84	Hydro.	10	Hydro.	–	–	38.9	38.9
WI22	47.2	1090	1.24	0	0	0	2.9	–	–	1.0
WI22	45.3	1113	1.24	0	0	0	6.6	–	–	2.2
WI22	46.5	1095	1.46	0	0	0	6.6	–	–	2.2
WI22	46.2	1122	1.55	0	0	0	7.9	–	–	2.6
WI22	46.0	1103	1.29	0	0 (wet)	0	5.1	–	–	1.7
WI22	46.5	1095	1.46	0	0 (wet)	0	5.6	–	–	1.9
WI22	44.9	1120	1.65	0	0 (wet)	0	6.5	–	–	2.2
WI22	46.3	1095	1.24	0	0 (wet)	0	5.2	–	–	1.7
WI23	37.1	1378	1.28	0	0	0	9.8	–	–	3.3
WI23	35.9	1536	1.52	0	0	0	9.3	–	–	3.1
WI23	39.2	1358	2.02	0	0	0	8.4	–	–	2.8
WI24	46.7	1172	1.28	0	0	0	5.2	–	–	1.7
WI24	46.3	1163	1.36	0	0	0	6.0	–	–	2.0
WI24	48.9	1167	1.28	0	0	0	5.8	–	–	1.9
WI24	47.3	1144	1.42	0	0 (wet)	0	4.8	–	–	1.6
WI24	46.8	1169	1.24	0	0 (wet)	0	5.2	–	–	1.7
WI24	46.4	1154	1.26	0	0 (wet)	0	4.6	–	–	1.5

(i.e., porosity change) was monitored using a pore pressure intensifier/volumometer.

5. Results

5.1. Benchtop elastic wave velocities

The measured dry P-wave velocity of the intact lava and ash tuffs is approximately 5 km·s^{-1} and between 1.2 and 3 km·s^{-1}, respectively (Table 2). We find that macrofractures within the lava can reduce the P-wave velocity to about 1.5 km·s^{-1} (Table 2). In general, the rocks containing higher porosities have lower P-wave velocities.

5.2. Uniaxial deformation experiments

Synopsis plots of the uniaxial stress–strain curves of the lava (WI20, Fig. 4a) and the ash tuff deposits (WI21, WI21b, WI22, WI23, and WI24; Fig. 4b–f) are presented as Fig. 4. The stress–strain curves are typical of those for rock in compression (Hoek and Bieniawski, 1965; Brace et al., 1966; Scholz, 1968). The curve is first concave upward (typically associated with microcrack closure) followed by a very nearly linear elastic

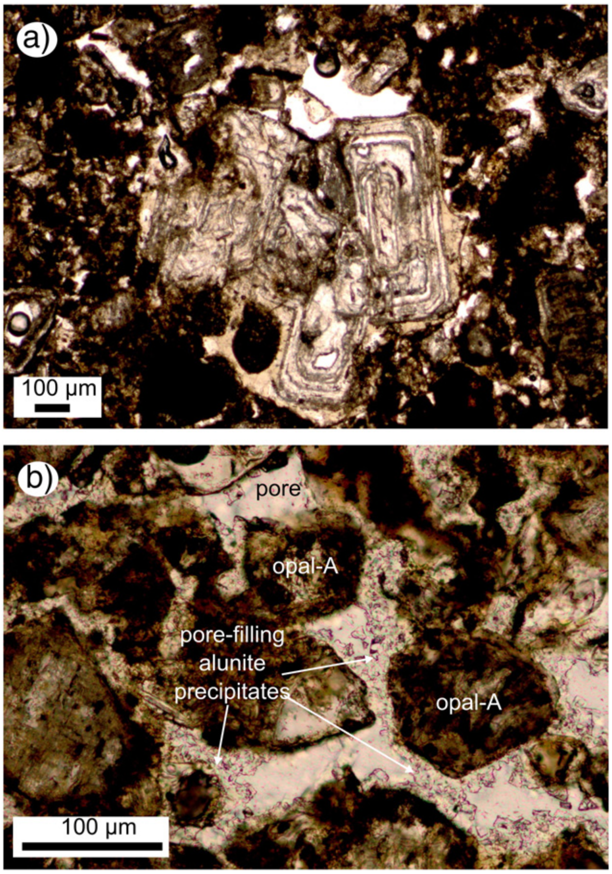

Fig. 3. Hydrothermal alteration. (a) Optical microscope image showing opalised crystals of feldspar that have retained their original shape (WI22). (b) Optical microscope image showing pore-filling alunite precipitates (WI21).

portion (recoverable or elastic deformation). In a third stage the curve departs from linearity as dilatant microcracks form (unrecoverable or inelastic deformation). Finally, a peak stress (the UCS of the rock) is attained before the rock succumbs to failure (typically axial splitting, see Fig. 5a and c), marked by a drop in stress.

A few global observations can be gleaned from these data. Firstly, the behaviour of each rock type can be described as macroscopically brittle (Rutter, 1986) or, as we will use in this study, "dilatant". Secondly, the lava (UCS = 44–140 MPa) is considerably stronger than the ash tuffs (UCS = 3–56 MPa). Thirdly, the range of UCS between samples from the block is quite large (a measure of the variability between samples). The large range in UCS for WI20 can be explained by the presence of macrocracks within the sample (see sample photographs in Fig. 4a). Fourthly, the gas elutriation pipes lowered the UCS of WI20 (from 56 MPa to 4–20 MPa). Finally, there appears to be negligible water-weakening (although it is difficult to assess due to sample variability). These uniaxial data are summarised in the plot of porosity versus peak stress (UCS) presented as Fig. 6. We note that sample strength is strongly dependent on the initial porosity, although it is difficult to separate this effect from the differences in alteration of the samples.

5.3. Triaxial experiments

The triaxial stress–strain, porosity reduction, and cumulative AE energy output curves for WI20 and WI21 are shown in Figs. 7 and 8, respectively. The data of Fig. 7 illustrate that the failure mode of WI20 remains dilatant up to our maximum effective pressure of 30 MPa. We observe dilatant behaviour (Fig. 7b), strain softening typically associated with macroscopic shear fracture formation (Fig. 7a), and an acceleration in AE energy output as failure is approached (Fig. 7c). Finally, we observe shear fractures in our deformed samples (Fig. 5b). The form of the stress–strain curves of Fig. 7a are qualitatively similar to the uniaxial stress–stain curves described above. The initial compaction of the samples (Fig. 7b) is the result of the closure of pre-existing microcracks, found to be abundant in this lithology (Fig. 2a). This is the cause of the pronounced concave upward portion of the stress–strain curves (Fig. 7a). The stress–strain behaviour is then very nearly linear: this is the elastic portion of the curve. A departure from linearity, strain hardening, is followed by the peak stress, strain softening, and ultimately sample failure via shear fracturing (Figs. 7a and 5b). The approach to sample failure is characterised by an increase in porosity (Fig. 7b) and AE activity (Fig. 7c). As effective pressure is increased (from 5 to 30 MPa), the peak differential stress (labelled "σ_p" on Fig. 7a) increases (from 138.4 to 254 MPa) and the strain-at-failure increases (from 0.6% to 1.5%).

Fig. 8 shows that the deformation of the ash tuff switches from dilatant (the blue curves) to compactant (the red curves) above effective pressure of 10 MPa, and that strain hardening occurs at an effective pressure of 30 MPa. The compactive stress–strain curves do not indicate strain softening (usually associated with macroscopic shear fracture formation) (Fig. 8a), and no shear fractures were observed in the deformed samples (Fig. 5e). Mechanical behaviour of this type is normally described as ductile (Rutter, 1986; Evans et al., 1990; Paterson and Wong, 2005). Ductility is the capacity of a material to deform to a substantial strain without the tendency to localise the flow into faults (Rutter, 1986), this description holds no mechanistic connotation. However, since ductile behaviour can be driven by microcracking (in the case of cataclastic flow; see Wong et al., 1997), which is brittle on the grain scale, and due to instances of compaction localisation (e.g., Baud et al., 2004), we have opted to refer to the failure mode in our experiments as simply "dilatant" or "compactant" (see also Heap et al., submitted for publication). We note however that, due to their high porosity, even the dilatant experiments (Peff = 5 and 10 MPa) experienced a net compaction at the end of the experiment (Fig. 8b). These experiments are interpreted as dilatant due to (1) failure is preceded by dilation (Fig. 8b) and, (2) failure is manifest as a shear fracture (Fig. 5d). The output of AE for the dilatant experiments do not show any significant acceleration as failure is approached and, during the compactant experiments, the output of AE was relatively steady throughout deformation (Fig. 8c). We also highlight that the total values of energy are much less than those required to induce shear fractures in the lava (Figs. 7c and 8c).

6. Discussion

6.1. Micromechanical processes

The operative micromechanical processes govern the mechanical behaviour and failure mode of rock. We have used a SEM to investigate the micromechanical processes responsible for the dilatant deformation in both the lava (WI20) and the ash tuff (WI21), and the compactant deformation in the ash tuff (WI21 and WI21b). SEM photomicrographs of samples of lava and ash tuff deformed in the dilatant regime are displayed in Fig. 9 (both at Peff of 10 MPa). Dilatational microcracks have coalesced to form a shear fault orientated at about 30–40° to the maximum principal stress (the Z-direction, see also Fig. 5a and c). We see that, in both cases, the damage zone surrounding the fault can reach 2–3 mm in width. The material is intact away from the fault damage zone (i.e., the deformation is localised).

The switch from a dilatant to a compactant failure mode also represents a switch in the predominant micromechanical process. The compactive deformation of the ash tuff is characterised by distributed pore collapse (Fig. 10a–d). The collapsed pores (about 100 μm in diameter) are bounded by microcracks and are often partially infilled with

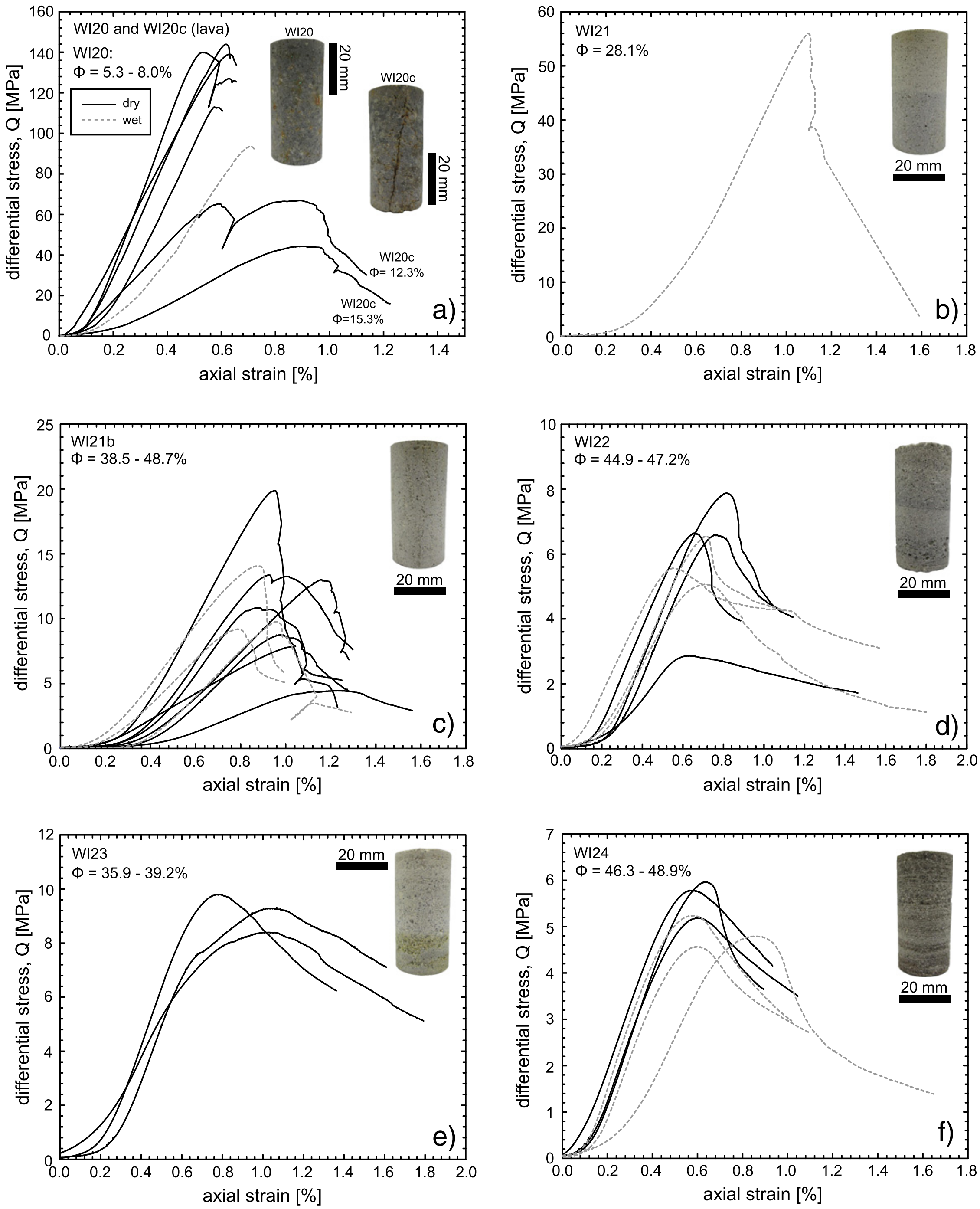

Fig. 4. Uniaxial stress–strain curves for the hydrothermally-altered rocks from Whakaari. Each graph contains the porosity range of the samples and a photograph of an intact sample. Dry and wet curves are shown in solid black and dashed grey, respectively. Note that the scales on the axes differ between the plots. Note: the porosity range quoted in panel (a) is for the non macrocracked samples only (i.e., WI20); the porosities of the two macrocracked samples (i.e., WI20c) are labelled next to the relevant stress–strain curve.

broken fragments. The progressive collapse of pores explains the substantial compaction and porosity loss during compactive deformation (Fig. 8b). For comparison, an intact pore is presented in the inset of Fig. 2b. In the case of WI21b, substantial pore collapse is seen within the gas elutriation pipes (Fig. 10e and f). Cataclastic pore collapse has previously been observed during the deformation of porous volcanic rocks at high confining pressures (Zhu et al., 2011; Loaiza et al., 2012; Adelinet et al., 2013; Heap et al., submitted for publication), highlighting the universality this mechanism as the operative micromechanical process driving low-temperature compactive deformation in porous volcanic rocks.

6.2. Failure envelopes for lava and ash tuff

The experimental data of this study can be summarised on a graph of differential stress (Q; i.e., σ_1–σ_3) required for failure versus effective mean stress (P, where $P = (\sigma_1 + 2\sigma_3) / 3 - Pp$) (Fig. 11; Table 2). In the dilatant regime, the peak stress (σ_p; see Figs. 7a and 8a) maps out the failure envelope (the circles in Fig. 11) whereas, in the compactant regime, it is the stress at the onset of shear-enhanced compaction C* (Wong et al., 1997) (see Fig. 8A) that delineates the compactive yield envelope (the squares in Fig. 11). In other words, the value of Q on the

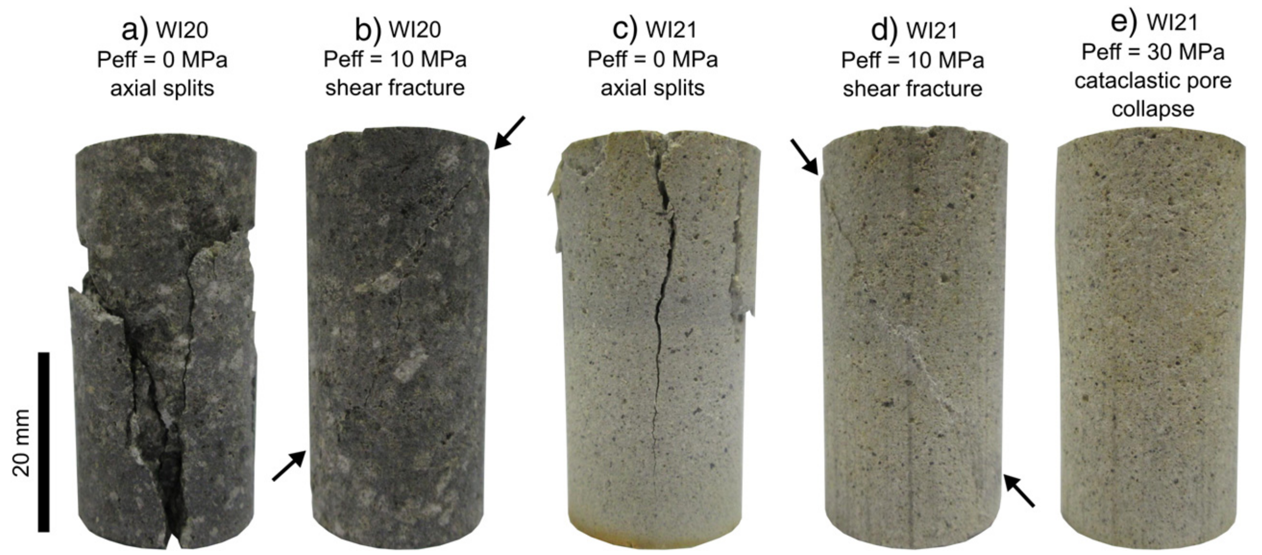

Fig. 5. Failure modes. (a) Sample of WI20 deformed under uniaxial conditions (Peff = 0 MPa) showing axial splits. (b) Sample of WI20 deformed under an effective pressure of 10 MPa showing a macroscopic shear fracture. (c) Sample of WI21 deformed under uniaxial conditions (Peff = 0 MPa) showing a large axial split. (d) Sample of WI21 deformed under an effective pressure of 10 MPa showing a macroscopic shear fracture. (e) Sample of WI21 deformed under an effective pressure of 30 MPa showing the absence of strain localisation; the sample exhibits mild barrelling.

P–Q diagram is given by the peak stress in the dilatant regime and by the onset of shear-enhanced compaction in the compactant regime; the value of P is simply calculated using the above relation, where σ_1 is the axial stress at failure (in the dilatant regime) or yield (in the compactant regime). The positions of C* were picked as the first deviation from elastic compaction in the porosity change curves (e.g., Fig. 8b). The positions of P*, the critical pressure for the onset of pore collapse under hydrostatic compression, plot along the *x*-axis (since Q = 0 MPa during these experiments). Failure (or yielding) occurs if the stress state of a particular rock plots outside the yield envelope (or cap); via shear faulting on the left hand side of the cap, and via pore collapse on the right hand side (see inset in Fig. 11c). The rock is intact (or pre-failure) inside the yield cap. Therefore, the larger the cap, the stronger, or more stable, the rock. We provide the failure envelopes for the lava (Fig. 11a) and ash tuff (WI21 and WI21b; Fig. 11b), together with data on tuff from the Alban Hills from Zhu et al. (2011), in Fig. 11. The data of WI21b were further separated into those containing porosities between 33–35% and 37–45%.

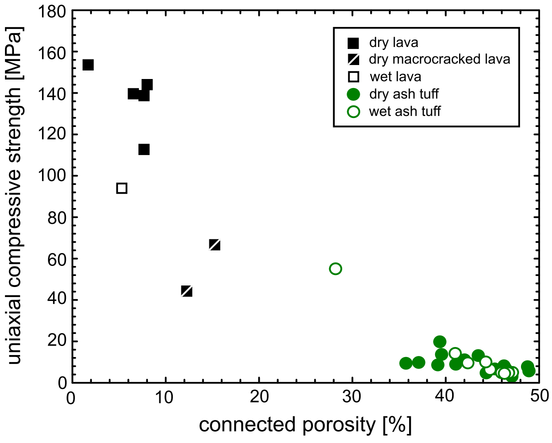

Fig. 6. The relationship between connected porosity and uniaxial compressive strength for the hydrothermally-altered rocks at Whakaari (data is available in Table 2). Dry experiments are denoted with filled symbols, and wet experiments with unfilled symbols.

Our lava experiments only delineate the dilatant failure envelope (a compactant failure mode was not observed under the implemented experimental conditions). We find that differential stress at failure increases linearly with effective mean stress (Fig. 11a), in accordance with the Mohr–Coulomb criterion. The ash tuffs also show that, in the dilatant regime, differential stress increases linearly with effective mean stress (Fig. 11b). The compactive yield envelope is parabolic, as is the case for porous sedimentary rocks (Wong and Baud, 2012) and some porous volcanic rocks (Zhu et al., 2011; Loaiza et al., 2012). We note that Heap et al. (submitted for publication) observed a linear compactive yield envelope for dual porosity andesites from Volcán de Colima (Mexico). The high initial microcrack densities of these andesites are thought to be responsible for the linear shape of the compactive yield envelope (see also Zhu et al., 2010). The ash tuffs of this study contain very low initial microcrack densities (no microcracks were observed in the SEM photomicrographs of Fig. 2), as was the case for the porous volcanic rocks of Zhu et al. (2011) and Loaiza et al. (2012). The C* data for the ash tuff containing 28–30% porosity can be well described by an elliptical cap. To define such an elliptical envelope, we employ the following expression, previously used to fit the onset of shear-enhanced compaction in porous sandstone (Wong et al., 1997; Fig. 11b):

$$\frac{(P/P^{*}-\gamma)^{2}}{(1-\gamma)^{2}}+\frac{(Q/P^{*})^{2}}{\delta^{2}}=1$$

where γ and δ represent the effective mean stress and the differential stress at the top of the ellipse normalised by P*, respectively (see Baud et al., 2006 for details). The δP* term could therefore be seen as the maximum differential stress that the rock can withstand before yielding. Previous studies on porous sandstones have reported values of about 0.5 for γ and δ ranging from 0.5 to 0.7 (Wong et al., 1997). In the case of ash tuffs from Whakaari, we find that γ and δ are equal to 0.3 and 0.65, respectively. The WI21b data between 33–35% porosity are equally well constrained by an elliptical cap of this form (Fig. 11b). Elliptical caps have been previously employed to accurately describe C* data of sandstones (Wong et al., 1997) and trachyandesite (Loaiza et al., 2012). Since our data can be described by the same elliptical cap, we have used the cap to extrapolate P* for the final and most porous ash tuff (WI21b with a porosity of 37–45%); we estimate a P* of about 27 MPa. This is slightly less than the 38.9 MPa required for a porosity

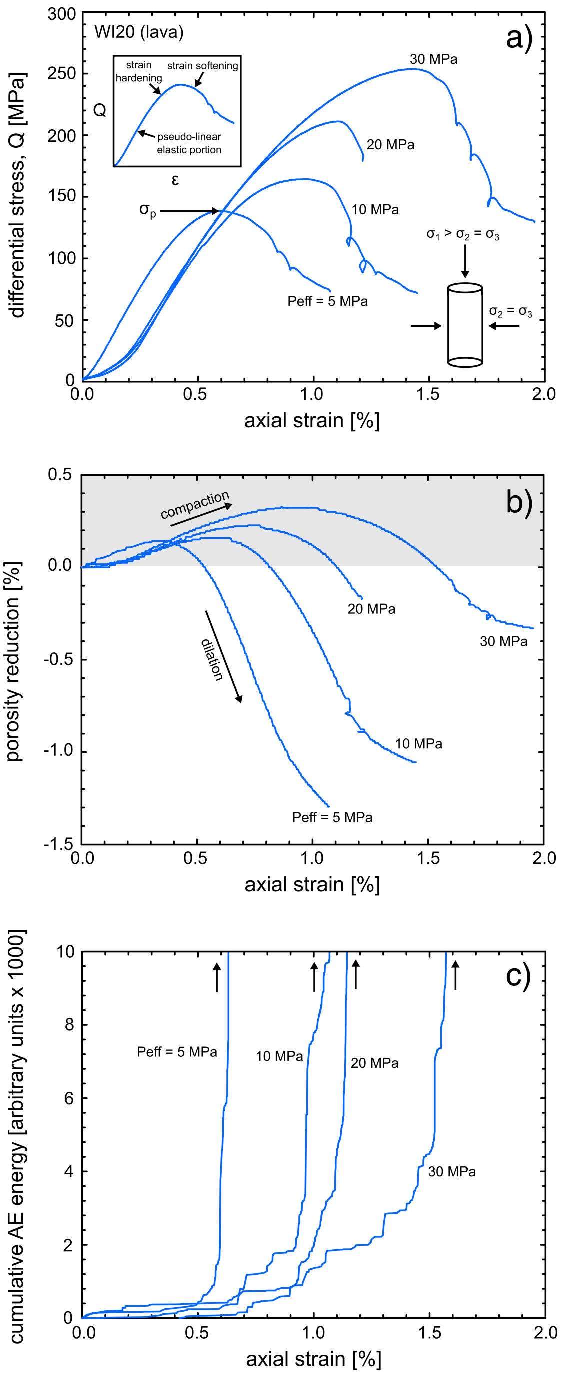

Fig. 7. Mechanical data from the triaxial experiments performed on the lava (WI20) at effective pressures (Peffs) between 5 and 30 MPa (the Peff is indicated next to each curve). (a) Stress–strain curves. The peak stress at failure (σ_p) is indicated for the experiment at Peff = 5 MPa. Inset shows one of the stress–strain curves with the main parts (the pseudo-linear elastic portion, strain hardening, and strain softening) labelled. Q—differential stress; ε—axial strain. (b) Porosity reduction curves for the experiments shown in panel (a). The grey area denotes net compaction and the white area net dilation. (c) Cumulative output of acoustic emission energy curves for the experiments shown in panel (a).

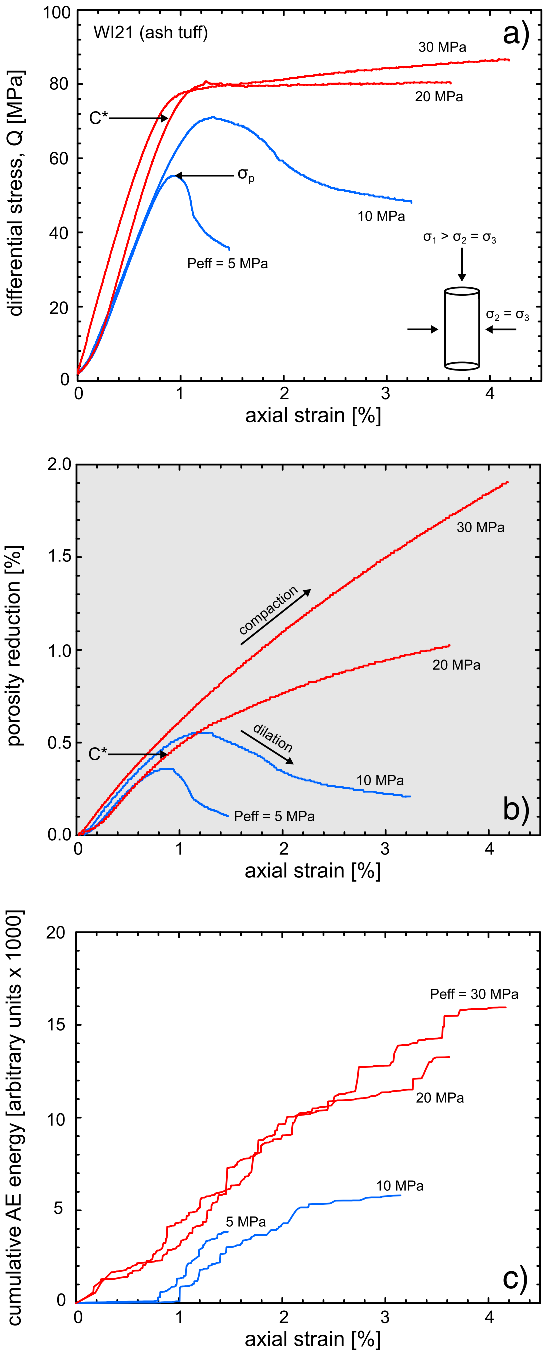

Fig. 8. Mechanical data from the triaxial experiments performed on the lava (WI21) at effective pressures (Peffs) between 5 and 30 MPa (the Peff is indicated next to each curve). (a) Stress–strain curves. The peak stress at failure (σ_p) is indicated for the experiment at Peff = 5 MPa. The differential stress at the onset of shear-enhanced compaction (C*) is indicated for the experiment at Peff = 20 MPa. (b) Porosity reduction curves for the experiments shown in panel (a). The grey area (i.e., the entire plot) denotes net compaction. The onset of shear-enhanced compaction (C*) is indicated for the experiment at Peff = 20 MPa. C: Cumulative output of acoustic emission energy curves for the experiments shown in panel (a). In all of the panels, dilatant experiments are in blue and compactant experiments are in red.

of 33–35%, and markedly lower than the 109.5 MPa required for the inelastic hydrostatic compaction of the ash tuff containing a porosity of 28–30%, thus highlighting the importance of porosity in controlling hydrostatic failure. We note that the failure envelope for tuff from Alban Hills containing a porosity of about 32% (from Zhu et al., 2011) is comparable to those for the Whakaari ash tuffs of a similar porosity (Fig. 11b). The synoptic plot of Fig. 11c highlights the large difference between the sizes of the caps for the lava and the ash tuffs. Therefore, the lava deposits are intact or stable over a much larger stress space. Our data also highlight that an increase in the porosity of the ash tuff can greatly reduce size of the yield caps and therefore the stress space within which the rock is intact (pre-failure). We anticipate that the

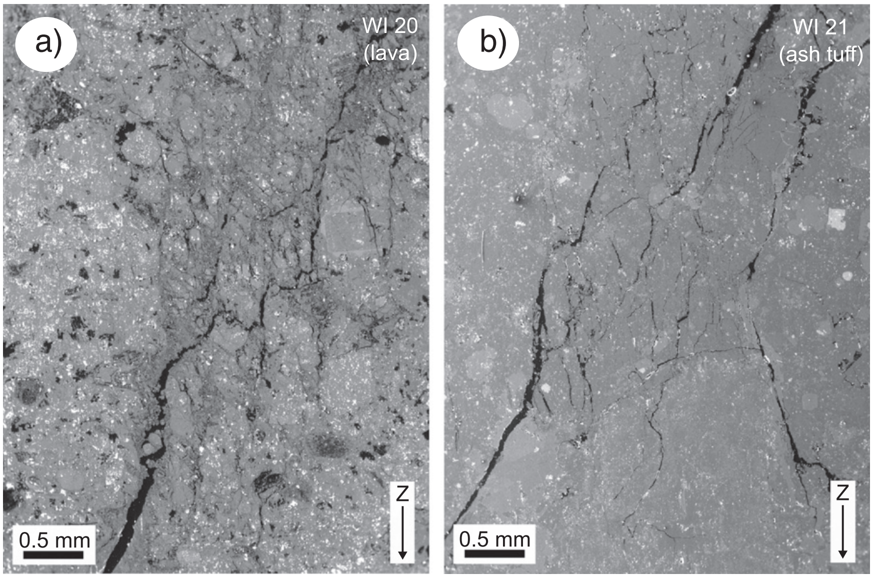

Fig. 9. Dilatant microstructures. SEM images of samples of lava (a) and ash tuff (b) deformed in the dilatant regime (at an effective pressure of 10 MPa). The direction of loading (the maximum principal stress) is in the Z-direction.

yield caps would be smaller for the ash tuffs containing a higher porosity (up to 50%, Table 2).

6.3. Influence of hydrothermal alteration on mechanical behaviour and failure mode

The rocks and deposits forming Whakaari are predominantly altered. Unfortunately, our samples do not contain the range of alteration required for a systematic assessment of its influence on the mechanical behaviour and failure mode of individual lithologies. However, our study does offer insights into the impact of alteration on rock mechanical behaviour. Pore-filling alunite, precipitated following complete devitrification (Fig. 3b), may increase the strength of the ash tuff by “cementing” the ash particles together and lowering the porosity. The data of this study support this assertion: the ash tuffs that contain alunite are less porous and stronger than the alunite-free ash tuffs (Table 2; Fig. 4). It is possible therefore, in regions of intense alunite precipitation, that the porosity of an otherwise compactant ash tuff could be sufficiently lowered to prompt a brittle response. We further speculate that it is unlikely that hydrothermal alteration will result in an increase in porosity sufficient to generate a compactant failure mode in the lava lithology studied here, especially considering the pore- and crack-filling nature of some of the alteration. However, without access to pristine materials, it remains unclear as to whether the initial devitrification of glass and replacement of crystal fragments with opal influences the failure mode, resulting in rock weakening or strengthening, or whether such chemical alteration plays a minor role when compared to porosity in controlling the mechanical behaviour and failure mode of these materials (see also Wyering et al., 2014).

6.4. Implications for Whakaari (White Island volcano)

Our study has shown that rock comprising the crater at Whakaari can react in contrasting ways to an applied differential stress. The low porosity lava responds in a dilatant manner (Fig. 7) and shear fractures form upon failure (Fig. 5b), accompanied with a large burst of AE activity (Fig. 7c). In addition, large differential stresses are required for macroscopic failure (Figs. 7a and 11). By contrast, the ash tuff deposits can respond in a compactant manner (Fig. 8). Deformation proceeds with low levels of AE activity and the resultant “damage” (cataclastic pore collapse, Fig. 10) is distributed throughout the sample (i.e., there is no shear fracture; see Fig. 5e). Failure in the compactant regime, the onset of shear-enhanced compaction, can occur at low differential stresses (Figs. 8a and 11).

Our experimental data help to constrain the depths (effective pressures) and differential stresses required for the two failure modes in the different lithologies. Here, using a schematic cross section for Whakaari (while we speculate that the subsurface stratigraphy consists of alternating layers of interbedded ash tuff and lava, as suggested by the exposed crater wall in Fig. 1c, we are certainly aware of the complexity of the volcano, see Cole et al., 2000), we use our experimental data to highlight where the different lithologies are likely to (1) be intact, (2) fail in a dilatant manner or, (3) fail in a compactant manner. We then discuss the implications of the failure mode on volcano deformation and stability, volcano seismicity, and outgassing.

Whakaari, as with many other hydrothermal volcanoes, is a dynamic system where the prevalent conditions (e.g., differential stress and pore pressure), influencing the mechanical response of the rock (Wong and Baud, 2012), vary as a function of time and space (e.g., Giggenbach and Sheppard, 1989; Bonafede, 1991; Bolognesi and D'Amore, 1993; Christensen and Wood, 1993; Day, 1996). To account for this in our cross-section (Fig. 12), we assume that the differential stress will be higher closer to active regional faults, intrusions, regions beneath high topography, and the active vents of the volcano (e.g., Jolly et al., 1994; Gerst and Savage, 2004; Roman et al., 2004). Secondly, we assume that effective pressure increases with depth. However, as Whakaari is an open system featuring circulating fluids (brines and/or gases) with extremely variable densities (depending on their phase, composition, depth, and proximity to a heat source), the pore pressure is likely to vary considerably (e.g., Fournier, 1991; Day, 1996). This, in turn, will influence the effective pressure; for example, rock close to a heat source, such as a magmatic intrusion, can experience a lower effective pressure due to the increase in pore pressure as a result of (1) the phase change of the pore fluid from liquid to vapour, which can create vapour-dominated zones at pressures above the local hydrostatic (Ingebritsen and Sorey, 1988) and, (2) the additional influx of magmatic fluids (Fournier, 1991), greatly aided by low permeability layers able to trap the fluids. Zones of elevated pore pressure are therefore most likely local (see also Fournier and Chardot, 2012). In addition, an overpressure can build if pore pressures can exceed the lithostatic pressure and may induce hydrofracturing. We have included zones of elevated pore pressure and pore overpressure, both close to a heat source, in our schematic

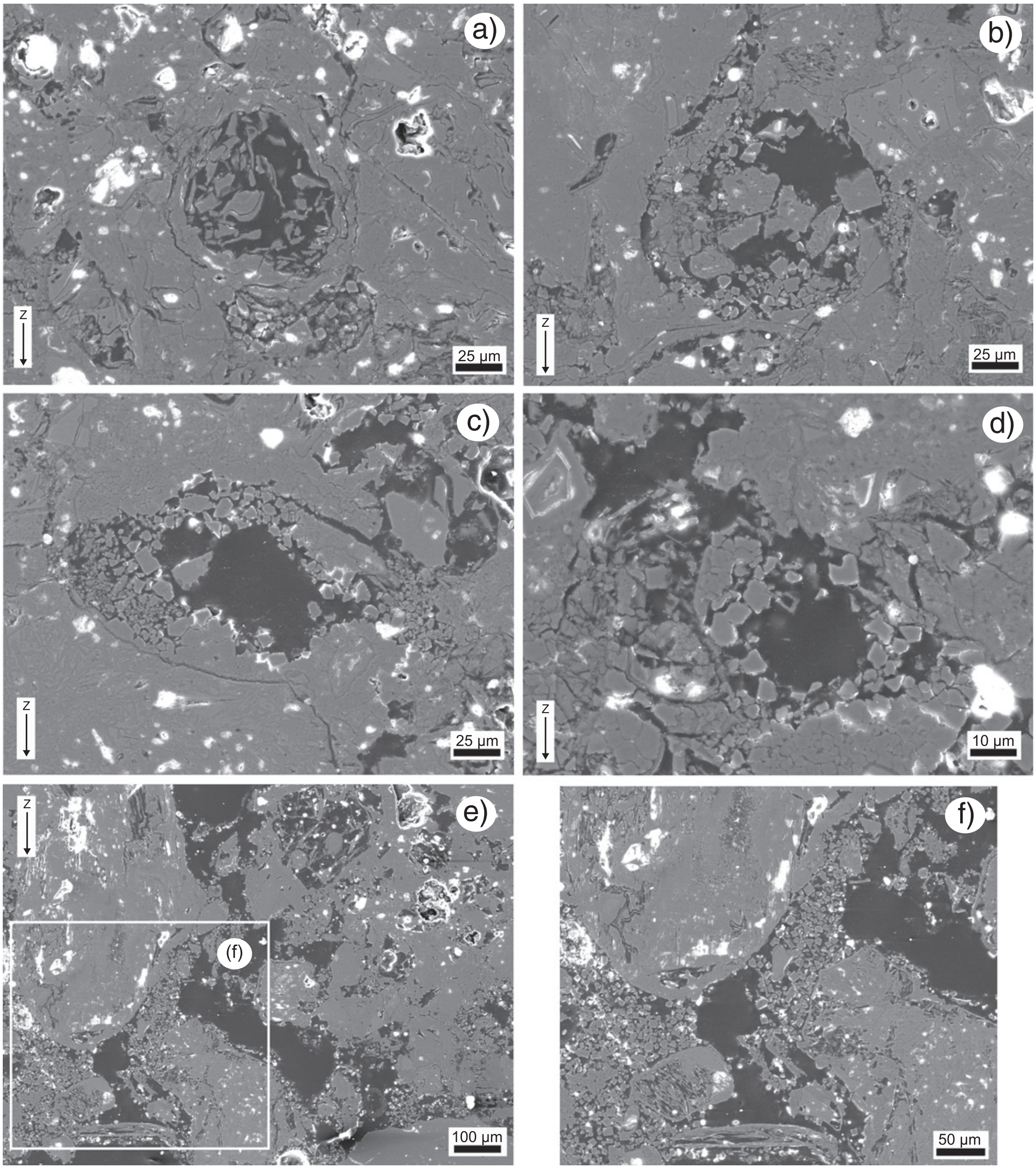

Fig. 10. Compactant microstructures. SEM photomicrographs of cataclastic pore collapse within an ash tuff sample (WI21) deformed in the compactant regime (at an effective pressure of 30 MPa, panels (a)–(d)). Pores are bounded by microcracks and are often partially infilled with broken fragments. Panels (e) and (f) show SEM images of a sample of WI21b deformed in the compactant regime (at an effective pressure of 30 MPa). Substantial pore collapse is seen within the gas elutriation pipes.

cross-section (Fig. 12). We again highlight that our experiments were performed at room temperature under varying pressure conditions, and therefore our schematic cross section focuses on the effect of effective pressure on the mechanical behaviour of rock. However, although the samples contain alteration assemblages representative of elevated temperatures, the direct effect of temperature on the mechanical properties of these rocks was not investigated here (although complementary investigations are underway).

6.4.1. Implications for deformation and volcano stability at Whakaari

Our schematic cross section of Whakaari is presented in Fig. 12. The lava, under the conditions relevant for the volcano, will react in a dilatant manner to stress (compactive failure is not anticipated). However, the stress and strain required for failure in the dilatant field increases with depth. Therefore, competent lava deposits far from regional faults, intrusions, and the active vent will be largely intact (Fig. 12); although we note that lava containing macroscopic fractures is weaker (Fig. 4). Only lava adjacent to sources of high differential stress will suffer shear fracturing (Fig. 12). By contrast, the ash tuffs are significantly weaker (Figs. 4 and 8; Table 2), and are therefore more likely to succumb to dilatant failure, even far from the sources of differential stress (Fig. 12). However, the ash tuffs will switch from a dilatant to a compactant mode of failure at effective stresses as low as 5 MPa (Fig. 8), equivalent to depths of about 250 m. Compactive failure, in contrast to dilatant failure, requires a progressively lower differential stress as effective pressure (depth) increases. Therefore, pore collapse and inelastic compaction in the ash tuff deposits is more likely as depth increases in the volcano. As a result, compactive behaviour can occur below 250 m close to the source of differential stress, and is still possible far from the source deeper in the volcano. The conditions for

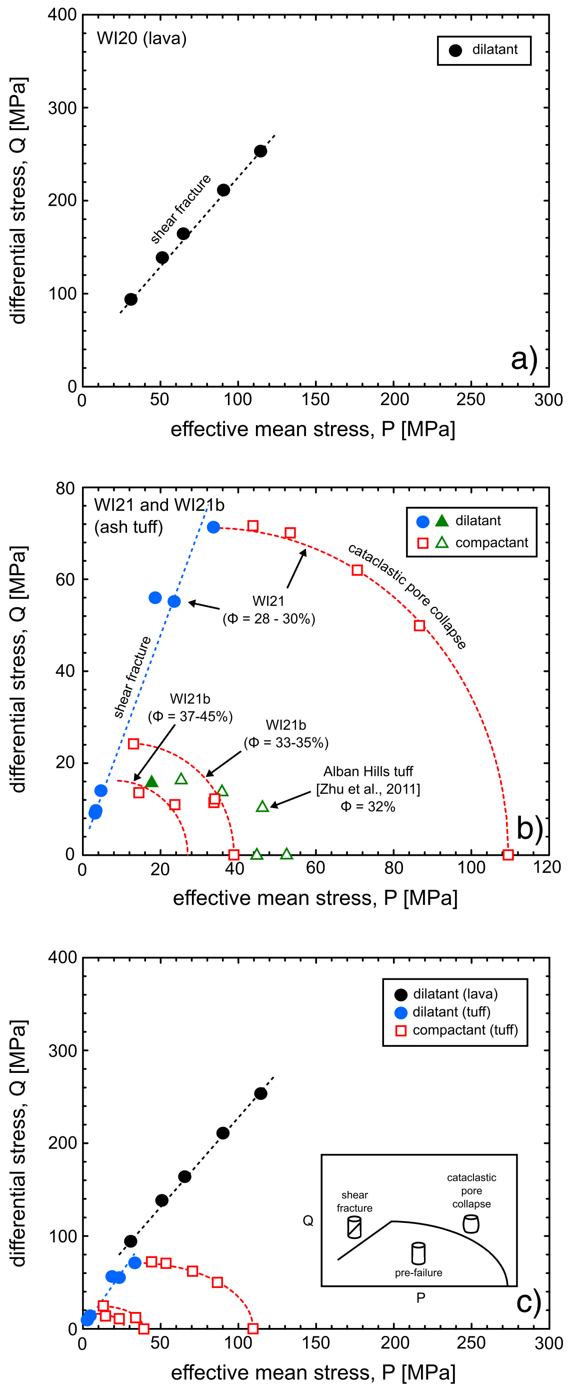

Fig. 11. Failure envelopes (in PQ space) for the lava (a) and an ash tuff (b). Dilatant experiments are denoted by the filled black (lava) and blue circles (ash tuff), and compactive yielding in the ash tuff by the unfilled red squares. Panel (b) also includes data from tuff from the Alban Hills, Italy (Zhu et al., 2011), represented by green triangles. Filled green triangle—dilatant experiment; unfilled green triangles—compactant experiments. (c) Synoptic plot containing both the lava and ash tuff data. The inset shows a cartoon explaining the influence of the different stress states on a rock inside and outside the failure envelope.

the inelastic compaction of the porous ash tuff are therefore satisfied for a large volume of the subsurface at Whakaari (Fig. 12). We also highlight that failure is possible in the ash tuffs in the absence of a differential stress. Our data show that inelastic hydrostatic compaction (failure in the absence of a differential stress) can occur at effective stresses as low at 27 MPa (porosity = 37–45%; Fig. 11) and will be lowered further for ash tuffs containing higher porosities (we highlight that some of our ash tuff deposits contained porosities approaching 50%, Table 2). We anticipate that hydrostatic failure in high porosity interbedded ash tuff could occur at depths as shallow as 2 km (Fig. 12). Inelastic hydrostatic compaction will not occur in the competent lavas under depths relevant for the volcano. An increase in pore pressure due to, for example, a proximal intrusion will locally lower the effective pressure (as depicted in our cross section; Fig. 12). A reduction in effective pressure will serve to weaken the dilatant lava, increasing the depth range where dilatant failure in the lava is possible, and promote dilatant failure in the ash tuffs at depth (Fig. 12). Further, higher pore pressure may be readily attainable where the ash tuff is bordered by low-porosity lava. The low-porosity lava could act as a low-permeability barrier, trapping fluids within the porous ash tuffs and allowing pore pressure to build (e.g., Fournier, 1991).

The failure modes seen at Whakaari have implications for ground deformation (e.g., Werner et al., 2008; Peltier et al., 2009; Fournier and Chardot, 2012) and the structural stability of the volcano (e.g., Lopez and Williams, 1993; Watters et al., 2000; Reid, 2004; Moon et al., 2005; Finn et al., 2007). The long term ground deformation pattern at Whakaari consists of inflation and deflation cycles (Peltier et al., 2009; Fournier and Chardot, 2012) that can be either localised or distributed over the crater floor (Werner et al., 2008). Inflation episodes are interpreted to be the result of an increase in pore pressure and the accumulation of magmatic volatiles (Werner et al., 2008; Peltier et al., 2009; Fournier and Chardot, 2012). However, deformation at Whakaari is dominated by subsidence (Peltier et al., 2009) and is interpreted as the net loss of materials (gas and magma). Our study intimates that the mechanical compaction of the interbedded ash tuff units will likely contribute to the overall trend of subsidence, volcano deflation, and net volume loss.

The structural stability of Whakaari is most likely jeopardised by shear fracturing (e.g., Moon et al., 2005), rather than distributed subsidence, although shear fractures and therefore the instability of the crater wall may be encouraged by compaction-driven subsidence. Our data, summarised in our schematic cross section (Fig. 12), show that the ash tuff will most likely undergo distributed pore collapse when exposed to a differential stress. The structural integrity of Whakaari is therefore most at risk from shear fracturing events within the competent lava deposits. Although the lava is strong, especially as depth increases, dilatant failure is possible close to sources of differential stress (faults, intrusions, active vents) and in areas of elevated pore pressure (Fig. 12; Day, 1996; Reid, 2004). Compaction-driven subsidence of the ash tuff units may contribute to volcano spreading (e.g., van Wyk de Vries and Borgia, 1996; van Wyk de Vries and Francis, 1997) and impart additional stresses to the lavas comprising the crater walls, increasing the likelihood of fracturing and landsliding. However, the stability of Whakaari may be enhanced as a result of the interbedded nature of the deposits comprising the subsurface (Figs. 1c; 12). Studies have shown that alternating layers of material with contrasting strength and stiffness may encourage dyke and fracture arrest (Gudmundsson, 2011 and references therein).

6.4.2. Implications for volcano seismology at Whakaari

Our study shows that the dry P-wave velocity of the intact lava and ash tuffs is about 5 km·s^{-1} (average = 4.83 km·s^{-1}) and between 1.2 and 3 km·s^{-1}, respectively, and that macrofractures, abundant within the lava, can reduce the P-wave velocity to about 1.5 km·s^{-1} (Table 2). In general, rocks containing higher porosities have lower P-wave velocities (as is typically the case, see Chang et al., 2006). Field estimates for the seismic velocities at Whakaari are 1.2 km·s^{-1} for the unconsolidated crater floor and 2.2 km·s^{-1} for the consolidated rocks of the crater wall (Jolly et al., 2012). Although we did not investigate the unconsolidated material in this study, we can confirm through our measurements (Table 2) that the P-wave

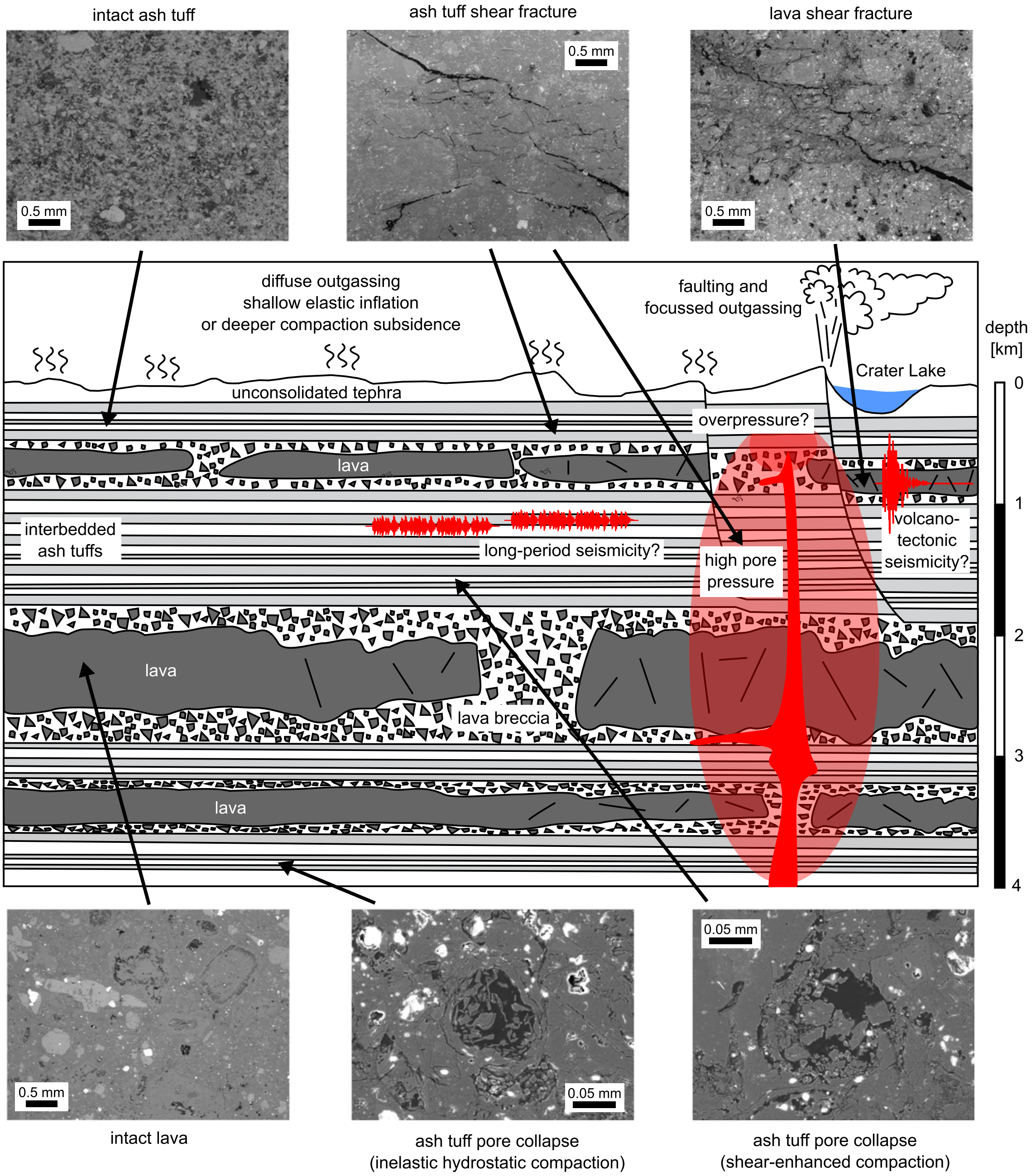

Fig. 12. A schematic cross section (depth 4 km) of Whakaari, New Zealand. The cross section is composed of interbedded ash tuffs and lava units (see Fig. 1c). We assume that differential stress is higher close to faults, intrusions, or active vents and that effective pressure increases with depth. We also provide a zone of elevated pore pressure, and therefore low effective pressure, close to an intrusion. We have highlighted zones, using our SEM photomicrographs (from Figs. 2, 9, and 10), in which the rocks will be either intact, have suffered dilatant failure, or have suffered compactive or hydrostatic failure. Also indicated are the possible source regions for volcano-tectonic and long-period or tremor-like seismicity. See text for details.

velocity of the most porous ash tuff (47% porosity) can be as low as 1.2 km·s^{-1}. The average velocity of the consolidated rocks comprising the crater wall is in general agreement with our data (sampled from the crater wall; Fig. 1c), supporting the notion that the subsurface crater wall is composed of partially lithified porous ash tuffs and fractured lavas.

The output of AE energy during our deformation experiments shows that mechanical failure of volcanic materials may produce seismogenic signals. The present study allows us to place some constraints on the possible source regions and deformation mechanisms that might produce the wide range of seismic signals observed in volcanic environments. Whakaari commonly produces the full range of seismic signals, including broad-spectrum volcano-tectonic earthquakes, long-period earthquakes, and both 1–5 Hz tremor and harmonic tremor (e.g., Nishi et al., 1996; Sherburn et al., 1998) as well as the lower frequency very-long-period (VLP) seismicity. The present work allows us to review these excitations in the context of the AE energy results. Our experiments showed that the high stresses required for dilatant failure in the lava samples generate high energy events (Fig. 7c), while the deformation of the ash tuff in both the dilatant and compactive regimes was accompanied by continuous, lower energy events (Fig. 8c). As a result, we suggest that local volcano-tectonic events are likely to originate within the lava, rather than the ash tuff deposits (Fig. 12). The large stresses required for dilatant failure in the lava may suggest that the earthquakes are the result of an increase in the local pore pressure (due to magmatic or hydrothermal activity), as suggested by Nishi et al. (1996). The rise in pore pressure will lower the effective pressure thus reducing the strength of the lava. Local pore pressure increases may be insufficient to fracture the lava when it is deeper and therefore stronger and may explain why volcano-tectonic seismicity typically occurs at depths less than 1 km (Nishi et al., 1996).

The more continuous, lower energy AE activity observed during the dilatant and compactive deformation experiments of the ash tuff is similar to the long-period seismicity or tremor-like signals. Recent work by Bean et al. (2014) suggests that long-period activity might be the result of weak slow-rupture brittle failure. Based on our data, we suggest that a combination of low energy dilatant failure and distributed cataclastic pore collapse (i.e., compactive deformation) could produce similar seismic signatures at Whakaari. One challenge to this notion is held in the apparent repeated nature of long-period seismicity at Whakaari, which implies a stationary non-destructive source process. If the seismicity emanates from a single source position, or a small number of source positions, it implies that the process of excitation is repeatable or may even occur as a continuous tremor signal. Hence, the energy release observed during the inelastic compaction of ash tuffs in this study may be a valid mechanism for a subset of long-period earthquakes, but seems unlikely for the specific class of repeating long-period signals.

Alternatively, the existence of broad-spectrum peaked tremor, which may occur spasmodically or as a persistent signal, may have a more distributed source volume, and hence may not indicate a repetitious source. In this case, an excitation mechanism including cataclastic pore collapse may occur. It is important to note that our proposed failure mechanism does not preclude the existence of other mechanisms, such as resonance in fluid-filled cracks or conduits (e.g., Julian, 1994; Chouet, 1996; Neuberg et al., 2000) but may instead explain the seismicity within a new candidate process. Significantly, we suggest that this process should be considered in the context of tremor excitations associated with magmatic intrusion/extrusion into cold shallow volcanic systems.

We highlight that long-period seismicity and volcanic tremors are inferred to have a shallow or sub-surface origin (Sherburn et al., 1998). Our triaxial data suggest that the switch from dilatant microcracking to distributed pore collapse is possible at effective pressures as low as 5 MPa (Table 2), or a depth equivalent to about 250 m (although such effective pressures can be achieved deeper in areas of high pore pressure), reinforcing our assertion that pore collapse may be a viable mechanism in the generation of the shallow long-period seismicity recorded at Whakaari. It must be noted however that our experiments were performed at room temperature. Fluctuations in temperature, of even a few hundred degrees, could impact the mineral composition (we note the presence of clays and hydrated sulphates, Table 1) and therefore the physical state of the rocks, and may thusly play an important role in the generation of the varied seismic events observed at Whakaari.

6.4.3. Implications for outgassing at Whakaari

The contrasting failure modes likely observed at Whakaari—dilatant or compactant—might influence style (focussed or diffuse) and the long-term efficiency of outgassing. Dilation and the formation of a shear fault in low porosity rocks are usually associated with an increase in permeability (e.g., Nara et al., 2011), whereas the compaction of high porosity rocks is usually associated with a decrease in permeability (e.g., Baud et al., 2012; Heap et al., submitted for publication). While outgassing at Whakaari is focussed through the crater lake (Werner et al., 2008), fed by fractures, and at a number of adjacent fumaroles, diffuse outgassing is also evident through the crater floor (Bloomberg et al., 2014), which may be explained by the data presented herein. The propensity for the ash tuff units forming the crater floor to deform in the compactive regime (i.e., without localisation) requires that the gases must diffuse through the network of interconnected pores, rather than along fractures (as is the case at crater lake). However, progressive porosity destruction, as a result of compactive deformation, may eventually reduce the permeability of the ash tuff units sufficiently to impede outgassing. In this eventuality, if the gases cannot find another means of escape, explosive behaviour may be encouraged due to the development of a high pore pressure.

7. Concluding remarks

This study has shown that hydrothermally-altered rock comprising Whakaari (White Island volcano) can react in contrasting ways to an applied stress. The low porosity lava deposits will react in a dilatant manner, and the high porosity ash tuff units can respond in a dilatant or compactant manner, depending on their depth. This switch in failure mode underlines a switch in the operative micromechanical process: dilatant behaviour is driven by dilatational microcracking and compactant behaviour by cataclastic pore collapse.

Our schematic volcano cross section emphasises that fact that different failure modes are possible within the volcano, depending on the prevalent conditions (differential stress, lithostatic and pore pressure, etc.). The choice of failure mode will impact the evolution rock physical properties (porosity, permeability, elastic wave velocity) and the seismicity accompanying periods of unrest. These data therefore have attendant implications for volcano seismicity, ground deformation, outgassing, and the structural stability of the volcano. For example, the compactive pore collapse of the ash tuffs, potentially prevalent in the subsurface at Whakaari, may explain the overall subsidence trend observed in ground deformation data (Peltier et al., 2009). The preference for shear fracture close to the active vent (in both the lava and ash tuff) and distributed pore collapse in the ash tuff away from the main vent (where the lava units are more likely to remain intact due to their high strength) may explain the localised outgassing at crater lake (Werner et al., 2008) and the diffuse outgassing on the crater floor (Bloomberg et al., 2014), respectively. The high energy AE events that accompany the dilatant failure of the lava (deformation of the tuff, in both the dilatant and compactant regimes, proceeds without forming high energy failure events) may apply some constraint on the source region (i.e., within lava at depths less than 1 km; lava at depth may be too strong to fracture without large increases in pore pressure) for shallow volcano-tectonic seismicity (Nishi et al., 1996). Further, the continuous low energy AE events during the compactive deformation of the ash tuffs may provide a mechanism for long-period seismicity or tremor-like signals observed at Whakaari (Sherburn et al., 1998; Bean et al., 2014). The data of this study are applicable to Whakaari, but could also shed light on the mechanical behaviour and failure modes of the rocks within active hydrothermal volcanoes worldwide.

Acknowledgements

The authors of this study acknowledge two Hubert Curien Partnership (PHC) grants: a Dumont d'Urville grant (number 31950RK) and a Procope grant (grant number 332065SG in France and 57130387 in Germany) funded and implemented by the New Zealand Ministry of Business, Innovation and Employment (MBIE), the Royal Society of New Zealand, the Deutscher Akademischer Austauschdienst (DAAD) in Germany, and the Ministry of Foreign Affairs (MAEDI) and the Ministry of Higher Education and Research (MENESR) in France. Funding for B. Kennedy was additionally provided by Marsden Fast Start (09-UO-017C) grant. B. Kennedy and Y. Lavallée thank the international science linkage funds from Royal Society of New Zealand (ISAT E613), the German Aerospace Centre (DLR) and the Federal Ministry of Education and Research (BMBF) (NZL 09/17). D. B. Dingwell acknowledges the ERC advanced grant “EVOKES” (explosive volcanism in the earth system: experimental insights, project number 247076). B. Scheu and K. Mayer acknowledge funding from the European Union's Seventh Program for research, technological development, and demonstration under grant agreement No 282759 (VUELCO). Y. Lavallée acknowledges funds from ERC starting grant “SLiM” (strain localisation in magmas, project number 306488). J. I. Farquharson acknowledges the Initiative d'Excellence (IDEX) funding framework. We gratefully acknowledge fruitful discussions with Paul Siratovich, Fabian Wadsworth, and Jim Cole. We also thank S. Bloomberg and N. Win for field assistance. We are thankful to Gilles Morvan for SEM assistance at Université de Strasbourg. Field access was provided by the Buttle Family, Pee Jay Tours, and the New Zealand Royal Air Force, in conjunction with GNS Science. This paper has benefitted from constructive reviews by Ludmila Adam and one anonymous reviewer.

References

Adelinet, M., Fortin, J., Schubnel, A., Guéguen, Y., 2013. Deformation modes in an Icelandic basalt: from brittle failure to localized deformation bands. J. Volcanol. Geotherm. Res. 255, 12–25.

Ayling, M.R., Meredith, P.G., Murrell, S.A.F., 1995. Microcracking during triaxial deformation of porous rocks monitored by changes in rock physical properties, I. Elastic-wave propagation measurements on dry rocks. Tectonophysics 245, 205–221.

Baud, P., Klein, E., Wong, T.-f., 2004. Compaction localization in porous sandstones: spatial evolution of damage and acoustic emission activity. J. Struct. Geol. 26, 603–624.

Baud, P., Vajdova, V., Wong, T.-F., 2006. Shear-enhanced compaction and strain localization: inelastic deformation and constitutive modeling of four porous sandstones. J. Geophys. Res. B: Solid Earth 111 (12) (art. no. B12401).

Baud, P., Townend, E., Meredith, P.G., 2012. Permeability evolution during triaxial compaction of an anisotropic porous sandstone. J. Geophys. Res. http://dx.doi.org/10.1029/2012JB009176.

Bean, C.J., De Barros, L., Lokmer, I., Métaxian, J.-P., O'Brien, G., Murphy, S., 2014. Long-period seismicity in the shallow volcanic edifice formed from slow-rupture earthquakes. Nat. Geosci. 7, 71–75.

Bergmann, J., Friedel, P., Kleeberg, R., 1998. BGMN—a new fundamental parameters based Rietveld program for laboratory X-ray sources, its use in quantitative analysis and structure investigations. CPD Newsl. 20, 5–8.

Bloomberg, S., Werner, C., Rissmann, C., Mazot, A., Horton, T., Gravely, D., Kennedy, B.M., Oze, C., 2014. Soil CO_2 emissions as a proxy for heat and mass flow assessment, Taupo Volcanic Zone, New Zealand (in revision).

Bolognesi, L., D'Amore, F., 1993. Isotopic variation of the hydrothermal system on Vulcano Island, Italy. Geochim. Cosmochim. Acta 57, 2069–2082.

Bonafede, M., 1991. Hot fluid migration: an efficient source of ground deformation: application to the 1982–1985 crisis at Campi Flegrei-Italy. J. Volcanol. Geotherm. Res. 48, 187–198.

Brace, W.F., 1964. Brittle fracture of rocks. In: Judd, W.R. (Ed.), State of Stress in the Earth's Crust. Elsevier, New York.

Brace, W.F., Paulding, B.W., Scholz, C.H., 1966. Dilatancy in the fracture of crystalline rocks. J. Geophys. Res. 71, 3939–3953.

Browne, P.R.L., 1978. Hydrothermal alteration in active geothermal fields. Annu. Rev. Earth Planet. Sci. 6, 229–250.

BS5930, 1999. Code of Practice for Site Investigations. British Standards Institution, London.

Çelik, M., Karakaya, N., Temel, A., 1999. Clay minerals in hydrothermally altered volcanic rocks, eastern Pontides, Turkey. Clay Clay Miner. 47, 708–717.

Chang, C., Zoback, M.D., Khaksar, A., 2006. Empirical relations between rock strength and physical properties in sedimentary rocks. J. Pet. Sci. Eng. 51, 223–237.

Chouet, B.A., 1996. Long-period volcano seismicity: its source and use in eruption forecasting. Nature 380, 309–316.

Christensen, B.W., Wood, C.P., 1993. Evolution of a vent-hosted hydrothermal system beneath Ruapehu Crater Lake, New Zealand. Bull. Volcanol. 55, 547–565.

Christensen, B.W., Mroczek, E.K., Kennedy, B.M., van Soest, M.C., Stewart, M.K., Lyon, G., 2002. Ohaaki reservoir chemistry: characteristics of an arc-type hydrothermal system in the Taupo Volcanic Zone, New Zealand. J. Volcanol. Geotherm. Res. 115, 53–82.

Clark, R.H., Cole, J.W., 1986. White Island. In: Smith, I.E.M. (Ed.), Late Cenozoic Volcanism in New Zealand. Royal Society of New Zealand Bulletin, pp. 169–178.

Cole, J.W., Thordarson, T., Burt, R.M., 2000. Magma origin and evolution of White Island (Whakaari) volcano, Bay of Plenty, New Zealand. J. Petrol. 41 (6), 867–895.

David, C., Wong, T.-f., Zhu, W., Zhang, J., 1994. Laboratory Measurement of Compaction-induced Permeability Change in Porous Rocks: Implications for the Generation and Maintenance of Pore Pressure Excess in the Crust. Pure and Applied Geophysics 143, 425–456.

Day, S.J., 1996. Hydrothermal pore fluid pressure and the stability of porous, permeable volcanoes. Geol. Soc. Lond., Spec. Publ. 110, 77–93.

del Portro, R., Hürlimann, M., 2008. Geotechnical classification and characterisation of materials for stability analyses of large volcanic slopes. Eng. Geol. 98, 1–17.

del Portro, R., Hürlimann, M., 2009. The decrease in the shear strength of volcanic materials with argillic hydrothermal alteration, insights from the summit region of Teide stratovolcano, Tenerife. Eng. Geol. 104, 135–143.

Eichelberger, J.C., Carrigan, C.R., Westrich, H.R., Price, P.H., 1986. Non-explosive silicic volcanism. Nature 323, 598–602.

Evans, B., Fredrich, J.T., Wong, T.-f., 1990. The brittle-ductile transition in rocks: recent experimental and theoretical progress. In: Duba, A.G., Durham, W.B., Handin, J.W., Wang, H.F. (Eds.), The Brittle–Ductile Transition in Rocks, The Heard Volume. ISBN: 0-87590-025-9, pp. 1–20.

Finn, C.A., Deszcz-Pan, M., Anderson, E.D., John, D.A., 2007. Three-dimensional geophysical mapping of rock alteration and water content at Mount Adams, Washington: implications for lahar hazards. J. Geophys. Res. 112, B10. http://dx.doi.org/10.1029/2006JB004783.

Fortin, J., Schubnel, A., Gueguen, Y., 2005. Elastic wave velocities and permeability evolution during compaction of Bleurswiller sandstone. Int. J. Rock Mech. Min. Sci. 42, 873–889.

Fortin, J., Stantchits, S., Dresen, G., Guéguen, Y., 2009. Acoustic emissions monitoring during inelastic deformation of porous sandstone: comparison of three modes of deformation. Pure Appl. Geophys. 166, 823–841.

Fournier, N., Chardot, L., 2012. Understanding volcano hydrothermal unrest from geodetic observations: insights from numerical modeling and application to White Island volcano, New Zealand. J. Geophys. Res. 117, B11. http://dx.doi.org/10.1029/2012JB009469.

Fournier, R.O., 1989. Geochemistry and dynamics of the Yellowstone National Park hydrothermal system. Annu. Rev. Earth Planet. Sci. 17, 13–53.

Fournier, R.O., 1991. The transition from hydrostatic to greater than hydrostatic fluid pressure in presently active continental hydrothermal systems in crystalline rock. Geophys. Res. Lett. 18, 955–958.

Fulignati, P., Gioncada, A., Sbrana, A., 1999. Rare-earth element (REE) behaviour in the alteration facies of the active magmatic–hydrothermal system of Vulcano (Aeolian Islands, Italy). J. Volcanol. Geotherm. Res. 88, 325–342.

Gerst, A., Savage, M.K., 2004. Seismic anisotropy beneath Ruapehu Volcano: a possible eruption forecasting tool. Science 306, 1543–1547.

Giggenbach, W.F., Sheppard, D.S., 1989. Variations in the temperature and chemistry of White Island fumarole discharges 1972–1985. N. Z. Geol. Surv. Bull. 103, 119–126.

Giggenbach, W.F., Shinohara, H., K. M., O. T., 2003. Formation of acid volcanic brines through interaction of magmatic gases, seawater, and rock within the White Island volcanic-hydrothermal system, New Zealand. Spec. Publ. Soc. Econ. Geol. 10, 19–40.

Gudmundsson, A., 2011. Rock Fractures in Geological Processes. Cambridge University Press, Cambridge.

Guéguen, Y., Palciauskas, V., 1994. Introduction to the Physics of Rocks. Princeton University Press, Princeton, New Jersey 9780691034522.

Heap, M.J., Farquharson, I.J., Baud, P., Lavallée, Y., Reuschlé, T., 2015. Fracture and compaction of andesite in a volcanic edifice. Bull. Volcanol. (submitted for publication).

Heap, M.J., Baud, P., Meredith, P.G., Vinciguerra, S., Reuschlé, T., 2014a. The permeability and elastic moduli of tuff from Campi Flegrei, Italy: implications for ground deformation modelling. Solid Earth 5, 25–44.

Heap, M.J., Lavallée, Y., Petrakova, L., Baud, P., Reuschlé, T., Varley, N., Dingwell, D.B., 2014b. Microstructural controls on the physical and mechanical properties of edifice-forming andesites at Volcán de Colima, Mexico. J. Geophys. Res. 119, 2925–2963.

Hoek, E., Bieniawski, Z.T., 1965. Brittle fracture propagation in rock under compression. Int. J. Fract. 1, 137–155.

Houghton, B.F., Nairn, I.A., 1989. A model for the 1976–82 phreatomagmatic and Strombolian eruption sequence at White Island volcano, New Zealand. N. Z. Geol. Surv. Bull. 103, 127–136.

Houghton, B.F., Nairn, I.A., 1991. The 1976–1982 Strombolian and phreatomagmatic eruptions of White Island, New Zealand: eruptive and depositional mechanisms at a 'wet' volcano. Bull. Volcanol. 54, 25–49.

Ingebritsen, S.E., Sorey, M.L., 1988. Vapor-dominated zones within hydrothermal systems: evolution and natural state. J. Geophys. Res. 91, 13635–13655.

Jaupart, C., 1998. Gas loss from magmas through conduit walls during eruption. Geol. Soc. Lond., Spec. Publ. 145, 73–90.

Jolly, A.D., Page, R.A., Power, J.A., 1994. Seismicity and stress in the vicinity of Mount Spurr volcano, south central Alaska. J. Geophys. Res. 99, 15305–15318.

Jolly, A.D., Chardot, L., Neuberg, J., Fournier, N., Scott, B.J., Sherburn, S., 2012. High impact mass drops from helicopter: a new active seismic source method applied in an active volcanic setting. Geophys. Res. Lett. 39, 12. http://dx.doi.org/10.1029/2012GL051880.

John, D.A., Sisson, T.W., Breit, G.N., Rye, R.O., Vallance, J.W., 2008. Characteristics, extent and origin of hydrothermal alteration at Mount Rainier Volcano, Cascades Arc, USA: implications for debris-flow hazards and mineral deposits. J. Volcanol. Geotherm. Res. 175, 289–314.

Julian, B.R., 1994. Volcanic tremor: nonlinear excitation by fluid flow. J. Geophys. Res. 99, 11859–11877.

Kennedy, L.A., Russell, J.K., Nelles, E., 2009. Origins of mount St. Helens cataclasites: experimental insights. Am. Mineral. 94, 995–1004.

Kyriakopoulos, K.G., Kanaris-Sotiriou, R., Stamatakis, M.G., 1990. The authigenic minerals formed from volcanic emanations at Soussaki, West Attica Peninsula, Greece. Can. Mineral. 28, 363–368.

Leybourne, M.I., et al., 2012. Submarine magmatic–hydrothermal systems at the Monowai Volcanic Center, Kermadec Arc. Econ. Geol. 107, 1669–1694.

Loaiza, S., Fortin, J., Schubnel, A., Guéguen, Y., Vinciguerra, S., Moreira, M., 2012. Mechanical behavior and localized failure modes in a porous basalt from the Azores. Geophys. Res. Lett. 39. http://dx.doi.org/10.1029/2012GL053218.

Lopez, D.L., Williams, S.N., 1993. Catastrophic volcanic collapse; relation to hydrothermal processes. Science 260, 1794–1796.

Manconi, A., Walter, T.R., Manzo, M., Zeni, G., Tizzani, P., Sansosti, E., Lanari, R., 2010. On the effects of 3D mechanical heterogeneities at Campi Flegrei caldera, southern Italy. J. Geophys. Res. B08405 http://dx.doi.org/10.1029/2009JB007099.

Miller, C.A., Jolly, A.D., 2014. A model for developing best practice volcano monitoring: a combined threat assessment, consultation and network effectiveness approach. Nat. Hazards 71, 493–522.

Moon, V., Bradshaw, J., Smith, R., de Lange, W., 2005. Geotechnical characterisation of stratocone crater wall sequences, White Island Volcano, New Zealand. Eng. Geol. 81, 146–178.

Mueller, S., Scheu, B., Spieler, O., Dingwell, D.B., 2008. Permeability control on magma fragmentation. Geology 36, 399–402.

Nara, Y., Meredith, P.G., Yoneda, T., Kaneko, K., 2011. Influence of macro-fractures and micro-fractures on permeability and elastic wave velocities in basalt at elevated pressure. Tectonophysics 503, 52–59.

Neuberg, J., Luckett, R., Baptie, B., Olsen, K., 2000. Models of tremor and low-frequency earthquake swarms on Montserrat. J. Volcanol. Geotherm. Res. 101, 83–104.

Nishi, Y., Sherburn, S., Scott, B.J., Sugihara, M., 1996. High-frequency earthquakes at White Island volcano, New Zealand: insights into the shallow structure of a volcano-hydrothermal system. J. Volcanol. Geotherm. Res. 72, 183–197.

Paterson, M.S., Wong, T.-F., 2005. Experimental Rock Deformation—The Brittle Field. Springer, New York 978-3-540-26339-5.

Peltier, A., Scott, B.J., Hurst, T., 2009. Ground deformation patterns at White Island volcano (New Zealand) between 1967 and 2008 deduced from levelling data. J. Volcanol. Geotherm. Res. 181, 207–218.

Pola, A., Crosta, G.B., Fusi, N., Barberini, V., Norini, G., 2012. Influence of alteration on physical properties of volcanic rocks. Tectonophysics 566–567, 67–86.

Pola, A., Crosta, G.B., Fusi, N., Castellanza, R., 2014. General characterization of the mechanical behaviour of different volcanic rocks with respect to alteration. Eng. Geol. 169, 1–13.

Procter, J.N., Cronin, S.J., Zernack, A.V., Lube, G., Stewart, R.B., Nemeth, K., Keys, H., 2014. Debris Flow Evolution and the Activation of an Explosive Hydrothermal System; Te Maari, Tongariro, New Zealand.

Read, M.D., Ayling, M.R., Meredith, P.G., Murrell, S.A.F., 1995. Microcracking during triaxial deformation of porous rocks monitored by changes in rock physical properties, II. Pore volumometry and acoustic emission measurements on water-saturated rocks. Tectonophysics 245, 223–235.

Reid, M.E., 2004. Massive collapse of volcano edifices triggered by hydrothermal pressurization. Geology 32, 373–376.

Reid, M.E., Sisson, T.W., Brien, D.L., 2001. Volcano collapse promoted by hydrothermal alteration and edifice shape, Mount Rainier, Washington. Geology 29, 779–782.

Roman, D.C., Moran, S.C., Power, J.A., Cashman, K.V., 2004. Temporal and spatial variation of local stress fields before and after the 1992 eruptions of Crater Peak Vent, Mount Spurr Volcano, Alaska. Bull. Seismol. Soc. Am. 94, 2366–2379.

Rutter, E., 1986. On the nomenclature of mode of failure transitions in rocks. Tectonophysics 122 (3–4), 381–387.

Scholz, C.H., 1968. Microfracturing and the inelastic deformation of rock in compression. J. Geophys. Res. 73, 1417–1432.

Sherburn, S., Scott, B.J., Nishi, Y., Sugihara, M., 1998. Seismicity at White Island volcano, New Zealand: a revised classification and inferences about source mechanism. J. Volcanol. Geotherm. Res. 83, 287–312.

Siratovich, P., Heap, M.J., Villenueve, M.C., Cole, J.W., Reuschlé, T., 2014. Physical property relationships of the Rotokawa Andesite, a significant geothermal reservoir rock in the Taupo Volcanic Zone. New Zealand. Geothermal Energy. 2:10.

Todesco, M., Rinaldi, A.P., Bonforte, A., 2010. Modeling of unrest signals in heterogeneous hydrothermal systems. J. Geophys. Res. 115, B09213. http://dx.doi.org/10.01029/02010JB007474.

van Wyk de Vries, B., Borgia, A., 1996. The role of basement in volcano deformation. Geol. Soc. Lond., Spec. Publ. 110, 95–110.

van Wyk de Vries, B., Francis, P.W., 1997. Catastrophic collapse at stratovolcanoes induced by gradual volcano spreading. Nature 387, 387–390.

Watters, R.J., Zimbelman, D.R., Bowman, S.D., Crowley, J.K., 2000. Rock mass strength assessment and significance to edifice stability, Mount Rainier and Mount Hood, Cascade Range Volcanoes. Pure Appl. Geophys. 157, 957–976.

Werner, C., Hurst, T., Scott, B.J., Sherburn, S., Christensen, B.W., Britten, K., Cole-Baker, J., Mullan, B., 2008. Variability of passive gas emissions, seismicity, and deformation during crater lake growth at White Island Volcano, New Zealand, 2002–2006. J. Geophys. Res. 113, B1. http://dx.doi.org/10.1029/2007JB005094.

Wong, T.-f., Baud, P., 2012. The brittle–ductile transition in rocks: a review. J. Struct. Geol. 44, 25–53.

Wong, T.-f., David, C., Zhu, W., 1997. The transition from brittle faulting to cataclastic flow in porous sandstones: Mechanical deformation. J. Geophys. Res. 102 (B2), 3009–3025.

Woods, A.W., Koyaguchi, T., 1994. Transitions between explosive and effusive eruptions of silicic magmas. Nature 370, 641–644.

Wyering, L.D., Villeneuve, M.C., Wallis, I.C., Siratovich, P.A., Kennedy, B.M., Gravley, D.M., Cant, J.L., 2014. Mechanical and physical properties of hydrothermally altered rocks, Taupo Volcanic Zone, New Zealand. J. Volcanol. Geotherm. Res. 288, 76–93.

Zhu, W., Wong, T.-f., 1997. The transition from brittle faulting to cataclastic flow: permeability evolution. J. Geophys. Res. 102 (No. B2), 3027–3041.

Zhu, W., Baud, P., Wong, T.-F., 2010. Micromechanics of cataclastic pore collapse in limestone. J. Geophys. Res. 115 (B4). http://dx.doi.org/10.1029/2009JB006610.

Zhu, W., Baud, P., Vinciguerra, S., Wong, T.-F., 2011. Micromechanics of brittle faulting and cataclastic flow in Alban Hills tuff. J. Geophys. Res. 116, B06209. http://dx.doi.org/10.1029/2010JB008046.